A THEORETICAL PERFORMANCE STUDY OF AN EXTERNAL CAVITY FIBER FABRY- PEROT INTERFEROMETER FOR DISPLACEMENT MEASUREMENT

by

Kumar Arumugam

A thesis submitted to the faculty of
The University of North Carolina at Charlotte
In partial fulfilment of the requirements
for the degree of Master of Science in
Mechanical Engineering

Charlotte

2015

Approved by:

____

Dr. Stuart T. Smith

____

Dr. Tony Schmitz

____

Dr. Tsinghua Her

ABSTRACT

KUMAR ARUMUGAM. A theoretical performance study of an external cavity
fiber Fabry- Perot interferometer for displacement measurement. (Under the direction of
DR. STUART T. SMITH)

The objective of this research is to explore a mathematical model developed by Wilkinson and Pratt for the external cavity fiber-based Fabry-Perot interferometer (EFPI) and to create a Michelson interferometer setup to validate a frequency modulation component of this model. A laser diode with nominal wavelength 635 nm is modulated by oscillating the diode current of maximum amplitude 22.62 mA to create correspondingly varying wavelength. Experiments are included to evaluate a rotating vector representation of the modulation harmonics in the signal received at the photodetector as of a cube corner translated by a piezo-electric actuator is displaced. Wavelength modulation as a function of diode current, the coherence length of the laser, and characteristics of the modulation harmonics are evaluated. A real time DAQ system and two lock-in amplifiers are utilized for detecting three side-band harmonics of the signal. For short range displacements this interferometer setup is monitored using a capacitance displacement sensor. The capacitance displacement measurement differed from the Michelson interferometer by 160 nm. The piezoelectric stage actuated with a 15 V Ramp signal produced 2.54 μm displacement of the cube corner. The setup is tested with Ramp signals of 75 V to 1.5 V and with the Ramp periods of 1 to 20 seconds to find the resolution of the interferometer, modulation of the wavelength sensitivity and the coherence length of the laser as 10.53 nm, 1.786 nm·A^{-1} and >1 m respectively. The best quadrature signal achieved corresponded to modulating the laser at amplitude of 18.86 mA at 1 kHz frequency with a path length difference of 6.35 mm. The amplitude comparison of side-band harmonics with Bessel function curves is consistent with a modulation amplitude of 1.28 rad corresponding to amplitude ratios of 0.5 (second and first) , 0.15 (third and second) and 0.06 (third and first) in the first through third Bessel function values.

ACKNOWLEDGEMENTS

I would like to thank my advisor Dr. Stuart T. Smith for his immense support and guidance throughout the spell of this research which broadened my horizon in the field of engineering. And I am also indebted to my parents for affording me this great opportunity and experience.

TABLE OF CONTENTS

LIST OF FIGURES

CHAPTER 1: INTRODUCTION

In the world of metrology, measurements of displacement vary from kilometers (km) to Pico meters (pm). The instrument measuring the distance gets complex as the requirements for accuracy and the precision increase. Optical interferometers are extensively used to measure those displacements with nanometer level uncertainties. The major types of interferometers used are Michelson and variants thereof and Fabry- Perot interferometer (FPI), whose principle of operation is explained below.

1.1. Michelson Interferometry- Principle

The Michelson interferometer setup is shown in FIGURE 1. It has two mirrors (or, equivalently, cube corners), one is static and the other is movable. The laser beam passing through the beam splitter, travels to the cube corners and will return to recombine at the beam splitter before reaching the photodetector. When the cube corner is moved, it changes the path length difference, $\Delta x = 2(x_1 - x_2)$ (since the beam travels to the cube corner and back, it covers the same optical path length twice) resulting in fringes observed at the photodetector. The fringes are the result of interference of the waves travelling to the photodetector, where the signals are sensed. When the displacement is equal to the integer multiple of the wavelength of light source (λ), complete fringes are formed. Therefore, the total displacement, $\Delta h = \frac{\Delta x}{2} = \frac{m\lambda}{2}$

Where, m is the total number of fringes observed.

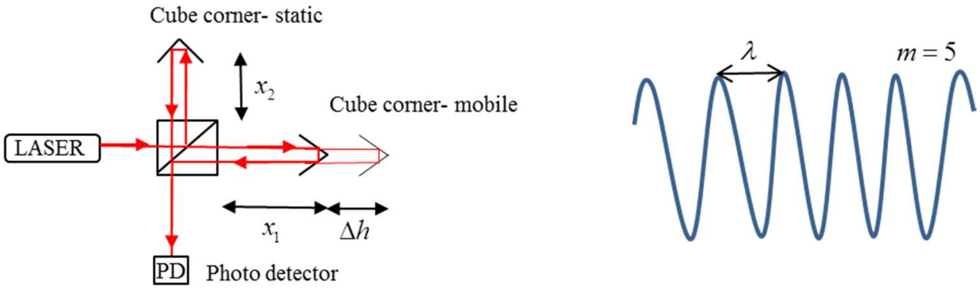

FIGURE 1: Michelson interferometry

2.1. Fabry- Perot Interferometry- Principle

The main difference between the Michelson and FPI is that the FPI does not use a beam splitter, which makes it more compact. Fabry- Perot interferometry works on the principle of multiple reflections between two partially reflecting surfaces. The light incident through the Mirror 1 hits the Mirror 2, part of which is reflected back due to the silvered mirror and that remaining is absorbed or transmitted out (FIGURE 2). The transmitted beams interfere due to the path length difference and forms fringes, used to measure the change in the gap between the mirrors from the mirror.

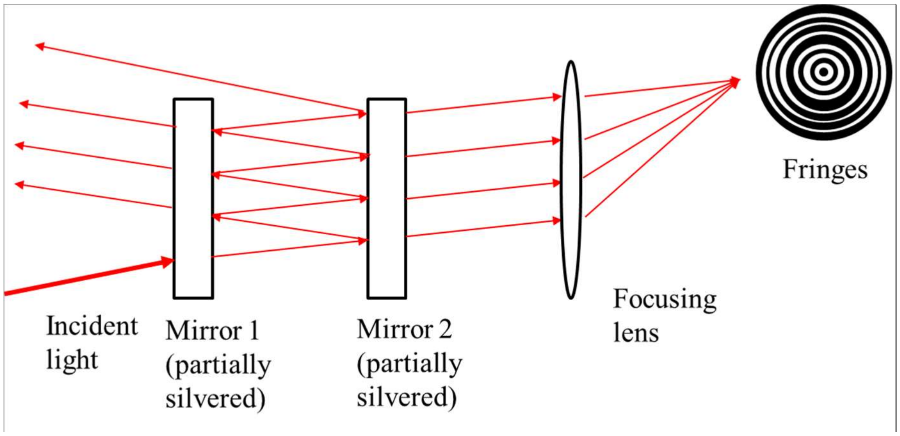

FIGURE 2: Fabry- Perot interferometry

1.2.1. Fiber Optic Fabry Perot Interferometer

The technique of Fabry- Perot interferometry is incorporated with an optical fiber. The fiber's ability to pass through confined spaces spanning millimeters makes the technique much efficient and makes remote interrogation possible. The measurement technique uses a fiber coupler having four ends (FIGURE 3). The first end receives the laser light from the source laser diode (VLM-635-03 LPA), two being the fiber output and the third one connecting to a photodetector. The laser output from the cleaved end of the fiber (acts as Mirror 1, shown in FIGURE 2) hits the target (Mirror 2, shown in FIGURE 2) surface mounted onto, or manufactured into the surface of the object being measured. In this technique we concentrate on the interference due to the inter-reflected beams.

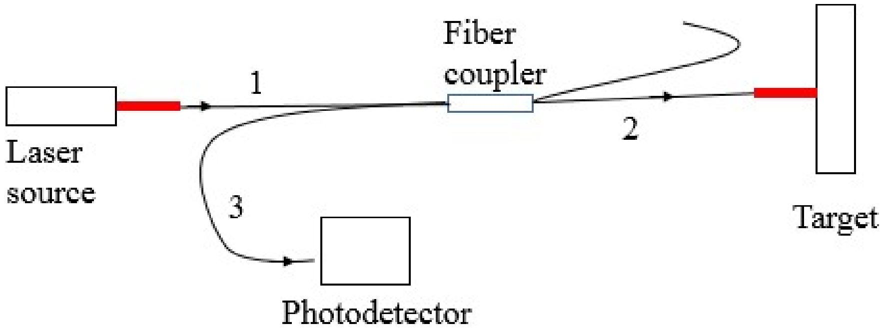

FIGURE 3: Fiber optic Fabry- Perot interferometer setup

The beam from the mirror surface reflects back to fiber end 2, this beam again reflects and interferes with another beam reflecting from the mirror surface. This beam gets coupled back in to the fiber, which is sensed by the photodetector. Interference of the multiple reflecting and diffracting beams plays a major role in shaping the characteristic of the reflectance from the cavity as a function of the separation between the fiber end face and the external reflecting mirror.

1.3. Literature Review

Wilkinson and Pratt did an analytical model for low- finesse, external cavity, fiber Fabry- Perot interferometers including multiple reflections and angular misalignment [1]. The fraction of electric field coupled back to the fiber is studied using a multiple reflection Fabry- Perot interferometer. Transverse, axial and angular offsets are considered. An analytical model for the reflectivity is derived and the phase information embedded in the Gaussian beam is taken in to account.

The model investigates reflectivity (R), parameters offset reflectance (Δ) and an interfering optical power (α) as a function of separation (z_m). The variables used in the experiments are: 1. the number of reflections ($N = 1, 5$) between the fiber and mirror, 2.

Perfect alignment and angular misaligned (angular offset, θ_m = 0.02°) of the fiber. The constants are mirror reflectivity ($r_m = 1$), spot radius (s = 3.7 μm), wavelength (λ = 1550 nm). An expression for Finesse is derived by considering angular misalignments and fiber coupling geometry alone. Scattering and transmission losses are neglected. Then, Finesse is related with varying z_m and θ_m.

The experiment used an uncoated glass fiber, with perfect cleave (assumed). A 5 axis manual fiber positioner is used in changing its position. In the series of experiments with N=1 and 5, the laser beam from the fiber hits mirrors of different reflectivity (r_m). 30 nm silver film ($r_m = 0.99\ e^{-i2.98}$), silicon wafer ($r_m = 0.55$) and glass ($r_m = 0.19$). The mirrors are displaced using a piezo electric actuator and cavity sweeps were performed for 80 μm. And the results are compared with the theoretical model developed. The asymmetric fringe shapes observed from the experiment are in accordance with the multiple reflection model developed.

Nowaskowski et al developed a miniature, multichannel, extended, range Fabry-Perot Fiber- Optic Laser Interferometer system for low frequency Si-traceable displacement measurement [2]. At the quadrature point (mid-point between the interference maximum and the minimum), intensity is sensed with respect to the displacement varying linearly with 1% error, and with the displacement range of 100 nm for the 1550 nm wavelength infra-red source used in these studies. Goal of this work is to build a laser interferometer displacement sensor with more range using the Fabry- Perot interferometer technique. The cleaved end of fiber and the polished specimen forms the two mirrors of the Fabry- Perot.

The laser wavelength which is modulated sinusoidally as the distance between the cavity changes. The measured spectrum of the signal has a carrier frequency f_0 and its sidebands f , $2f$ with f being the modulation frequency. The intensity of f (I_f) and $2f$ (I_{2f}) are combined as a rotating vector with displacement, this gives the value of phase angle, $\alpha = \tan^{-1}\left(\frac{I_{2f}}{I_f}\right)$.

The displacement of the polished surface is,

$$\Delta h = \frac{\lambda}{2}\left(\frac{\alpha}{360^{\mathrm{O}}} + n\right) \tag{1}$$

Where,

n is the number of full rotations of the vector.

By tuning the laser wavelength, first (λ_1) and last value (λ_2) of the laser wavelength in the cavity is used to find the absolute cavity length by the formula

$$h = \frac{m}{2}\left(\frac{\lambda_1\lambda_2}{\lambda_2 - \lambda_1}\right) \tag{2}$$

Where, m is the number of interference cycles.

Following are the three error compensation techniques applied because of the periodic errors in the system:

1. The curve fit of analytical approach by Wilkinson et al is performed with experimental results which deviate by 1%.
2. The cavity is swept 35 μm to find the error between the idealized and the measured angle of the vector. This data set creates a 7200 point look up table for

error correction, a technique also used by Thurner et al. Usage of this technique reduces the error to nanometer level.

3. The amplitude variation of *f* and *2f* signals acts as another source of error. A PID system in combination with a lock-in amplifier and Field Programmable Gate Array (FPGA) is incorporated to maintain the modulation depth value, thereby keeping the amplitude ratio of the *f* and *2f* signals at unity.

To test the stability of displacement the cavity is formed between fiber held in a ferrule and the glass wedge and the setup is glued on Zerodur taking advantage of its very low coefficient of thermal expansion and experiment is performed in temperature controlled chamber for 60 hours to find that the average stability is 1nm per 24 hour.

The maximum range of the sensor and the maximum misalignment angle achieved are 25mm and ±10° respectively.

Eric D. Black's paper on the introduction to Pound- Drever- Hall laser frequency stabilization [3] explains about locking the laser frequency. The frequency of the laser is measured using Fabry Perot interferometer and it is fed back to the laser to stabilize the frequency.

The closed loop control of the laser signal is constructed as follows: Frequency of the laser is modulated using Pockels cell (FIGURE 4) and passed through the optical isolator and hits the reflecting surface (cavity). The reflected light from optical isolator is detected by the photo detector. The optical isolator plays a major role in restricting the reflected light from entering back in to the laser source, which stops the laser frequency getting unstabilize. The light from the photo detector is sent to the mixer which uses a phase shifter. The mixer compares it with the oscillator's signal and then, the low pass filter separates the lower frequency signal and passes it through servo amplifier to lock the laser in the tuning port.

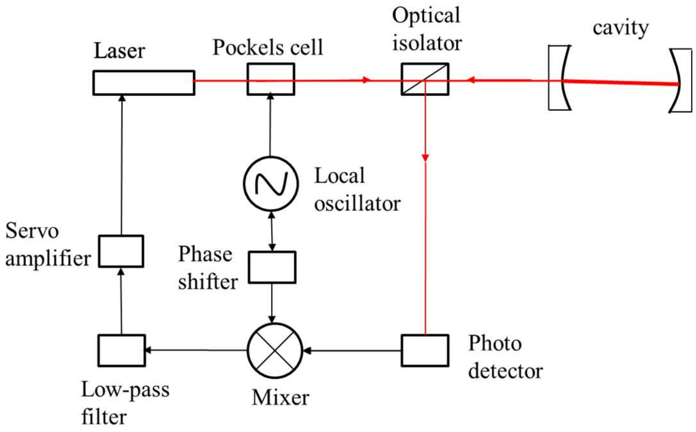

FIGURE 4: Layout for locking the cavity to laser

Modulating the frequency of laser produces side bands, which interferes with the reflected beam to produce beat patterns. This beat pattern tells us the phase of the reflected beam. The conceptual model is quantified with slow modulation and fast modulation. The error signal is plotted with the frequency found, which is used to control the frequency noise.

Thurner et al has done the absolute distance sensing using two laser optical interferometry [4]. The authors have combined the use of frequency tuning interferometric technique with dual wavelength interferometry. A fiber-optic Fabry- Perot interferometer with two laser sources is used in the experiments.

The change in wavelength causes the phase difference proportional to optical path length. This principle is used to sweep Laser A by $\Delta\lambda$ to find the coarse absolute distance x_{fti}.This procedure has a µm uncertainty due to the movement of target, So Laser B is used to perform wavelength sweep to track the target to correct the value of x_{fti}.

Number of integers of beating wavelength calculated using x_{fti} is used to determine an intermediate coarse value of initial absolute distance, $X_{\Lambda s}$ Finally, $X_{\Lambda s}$ is used to determine the interference order of one of the wavelength, which in turn is used to calculate the high precision absolute distance.

Instrumentation of the process is as follows: The light from two laser sources (whose wavelengths are feedback controlled with the current and temperature variables) are mixed and sent to the fiber through the fiber coupler. The end of fiber and the highly reflecting mirror (target) acts as the two reflecting surfaces of interferometer. The light reflected from the target interferes with reference light, and it is detected using InGaAs detector, which gives a beating interference pattern when the target is moved.

The laser signals A and B are separated and their interference phases are recovered without using optical filters. The lasers A and B are frequency modulated with frequencies ω_a and ω_b. The superposition occurs with these two signals and is detected by the detector. The interference phases Φ_a, Φ_b are determined by lock-in demodulation, followed by normalization of signal amplitudes and determination of tangents between ω and 2ω components. The signals thus obtained are the first and second harmonics of carrier frequency. The interference phase measured using the detector is non-linear but it deviates periodically as a function of displacement. Look-up tables are then used to correct the periodic nonlinearities.

The wavelengths are stabilized using two low pressure gas cells (Acetylene) using feedback PID to measure the absolute distances as it cannot be ensured only by current and temperature stabilization.

The result has the maximum uncertainty of ± 3 nm. The statistical improvement is made by interchanging the Laser sources A and B. And to demonstrate that the position of the stage can be found at any instance of time, the interferometer is switched off for a particular period and turned back on. The results obtained show nanometer repeatability of the absolute gap over a range of sub-meter.

Feng et al. have explained Physical origin of the Gouy phase shift, [5]. The presence of transverse components of the wave vector k_x, k_y reduces the axial component of the wave vector k_z of the diverging beam propagating along z direction. This results in Gouy phase shift. The Gaussian transverse distribution is used in Fourier transform and normalized to express Gouy phase shift for real and complex values of beam radius. Rayleigh length, z_R plays a major role in shaping the beam radius ω. Hermite- Gaussian beam equation is used to derive the phase shift for higher order transverse modes.

Rasool et al have developed a low noise all- fiber interferometer for high resolution frequency modulated atomic force microscopy imaging in liquids [6]. A Fabry-Perot interferometer is used as a deflection sensor for Frequency Modulated- Atomic Force Microscopy imaging in liquid environment. In the system, 2 X 2 coupler is replaced using the Fiber optic circulator, which results in less laser noise at photo detector. The piezo electric stack is used to calibrate the sensor before every experiment, to keep the average distance between the fiber end and cantilever constant where the slope of the fringe pattern is the maximum.

Noise factors such as PD shot noise, voltage noise, and effective deflection noise density are discussed. Reflected power of 4 different reflectivities is plotted as a function of cavity distance with varying reflectivity and the incident power. Sensor is optimized to achieve low deflection noise density caused by the photo diode shot noise. Deflection noise density increased with the uncoated fiber in water, due to the change in refractive index.

The mathematical model agrees with the experiment involving dielectric coated fiber face and silicon wafer with 30 nm thick gold coating. The fringe visibility is found to be higher in water than in air, because of the high coupled power. The high resolution image of cleaved muscovite mica sample under water is obtained using the FP technique, as the maximum sensitivity point is picked and maintained with feedback circuits.

Hunger et al. have developed a fiber Fabry- Perot cavity with high finesse [7].The fabrication of concave mirrors on optical fibers using the single pulse of Co2 laser is studied. AFM and SEM are used to analyze the surface. Curve fit of the machined surface is performed with Gaussian profile.

Fiber face's surface roughness, S is calculated using the scatter loss, σ_{sc} and wavelength of light, λ. Maximum finesse value expected is 130000.

$$S \approx \left(\frac{4\pi\sigma_{sc}}{\lambda} \right)^2 \tag{3}$$

And the following concepts are discussed

1) Parameters to reduce the waist radius, ω_0 of the beam.

2) Coupling efficiency, ϵ is related in terms of cavity mode radius w_m and Gaussian transverse mode profile radius w_f, with the assumption that the mode is well aligned with fiber axis.
3) A model to attain maximum cavity length (useful in introducing membrane like objects or to reduce free spectral range) with negligible clipping loss is discussed. Cavity quantum electrodynamics (CQED) parameters like Single photon coupling rate (g), FWHM (k), Finesse and Quality factor are related with length of the cavity (L). Wavelength of the laser used is 780 nm. Results show that the Finesse and Quality factor decays after L > 75 μm (approx.) and g, k decreases throughout as L increases.
4) Experiments on Cu alloy coated single mode and Multimode fibers are carried out. The losses of FFPC due to the coating are measured. Then the Optomechanical bistability due to local heating caused by mirror coating is discussed. Using the finite element simulation, the absorption loss due to the SiO2 and Ta205 coating layers is calculated which matches the experimental results.
5) The fibers inserted to ferrules are mounted on to the micro positioning stages to measure Finesse with the cavity length change. Shear piezo electric actuators are used in alignment of fibers, and the alignment was observed using stereo microscope. Maximum finesse value achieved is 37000 ± 5000.
6) The laser is modulated with sidebands of ±500 MHz for frequency calibration. Then the lasers with frequency difference of 212 MHz are used to measure the dependence of polarization of incoming beam.

Nemoto et al have analyzed the splice loss in single- mode fibres using a Gaussian field approximation [8]. The splice loss due to the transverse, longitudinal and angular misalignments is analyzed when two fibers F1 and F2 are positioned. The transverse field distribution of the fundamental mode in the fiber is approximated by Gaussian profile. By relating the rectangular and cylindrical co-ordinate systems, the formula for coupling coefficient, C and Power transmission coefficient, T (coupling efficiency) between the Gaussian beam and the fundamental mode in the fiber F2 are derived.

Numerical examples of the truncated surfaces of different type of fibers are studied in the presence of air and matching oil in the gap between the fibres F1 and F2. Results implies that the effects of misalignment which reduces T in step index fibers are larger than the parabolic index fibers. Whereas, when angular misalignment alone is present, the loss in parabolic index fibers is larger than step index fibers.

The presence of matching oil increases T for the separation (z) but decreases for tilt angle (θ). When the parameter specifying index gradient (α) increases, T_x and T_z decreases and T_θ increases.

Theoretically calculated T , considering the power transmission coefficient in the gap T_g is compared with experimental results obtained by varying separation and offset. Analysis of this paper is adapted by Wilkinson and Pratt in their model [1].

CHAPTER 2: THEORETICAL STUDIES

2.1. Inter Reflection between Fiber and the Target

The transmission, reflection coefficients inside and outside (cavity) the fiber is represented as t_0 , r_0 and $t_0^{'}$, $r_0^{'}$ respectively. FIGURE 5 shows that the light is emitted in to fiber (wavelength, λ) with initial intensity, I_0, Part of the light gets reflected from the inside face of the fiber and has a reflection coefficient of r_0 and part of it transmits outside with the transmission coefficient of $t_0^{'}$. This transmitted beam hits the target's surface with the mirror reflectivity of r_m , part of it gets reflected from the target with a reflection coefficient of $r_0^{'1}$ and part of it gets transmitted through the target as $t_{01}^{'}$. The beam with reflection coefficient of $r_0^{'1}$ hits the face of the fiber. Part of $r_0^{'1}$ gets transmitted back in to the fiber with transmission coefficient, t_0 and another part is reflected back with the reflection coefficient of $r_0^{'2}$. Thus subsequent inter-cavity reflections occur. The intensity of the light coupled back in to the fiber for first two cycles (n = 1 and 2) are $I_1 = I_0 r_m t_0^{'} t_0$ and $I_2 = I_0 r_m^{2} r_{01}^{'} t_0^{'} t_0$, which is equivalent to the summation term in equation (4) for infinite reflections. The theoretical model used the equations of Wilkinson et. al. [1]

Resultant reflection coefficient of the cavity, $r = r_0 C_{n=0} + t_0 t_0^{'} \sum_{n=1}^{\infty} (r_m^{n} r_0^{'n-1}) C_n$ (4)

For uncoated glass fiber aligned against a solid, dielectric surface and a cavity of air, reflection coefficient is given by (equation 14 in Wilkinson et. al [1])

$$r = r_0 C_{n=0} + \frac{t_0^2}{r_0} \sum_{n=1}^{\infty} (r_m r_0)^n C_n e^{-i\pi} \tag{5}$$

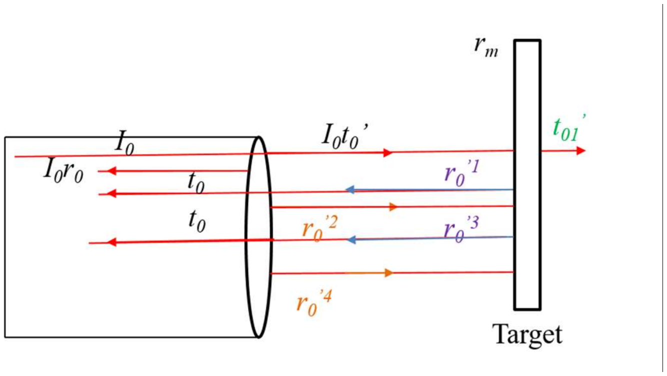

FIGURE 5: Inter- reflection between the fiber face and target

FIGURE 6 shows a model for mirror's angular misalignment (θ_m), transverse offset (x) and separation (z) of the target mirror.

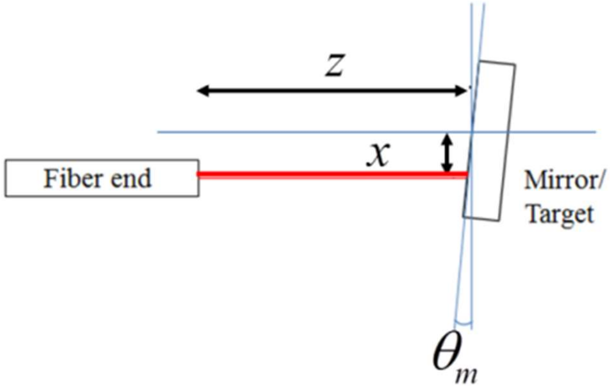

FIGURE 6: Mirror misalignment

Considering these misalignments, the intensity of the light coupled back to the fiber for N reflections (equation (6)) is given by squaring equation (5) (equation 15 in Wilkinson et. al [1]). This intensity is detected by the photodetector shown in FIGURE 3.

$$R = r_o^2 + \frac{t_o^4}{r_o^2}\sum_{n=1}^{N}(r_m r_o)^{2n}\Lambda_n^2 + 2t_o^2\sum_{n=1}^{N}(r_m r_o)^{2n}\Lambda_n\cos(\beta_n + \Theta_n + \pi) +$$
$$2\frac{t_o^4}{r_o^2}\sum_{l=1}^{N}\sum_{n=l+1}^{N}(r_m r_o)^{n+l}\Lambda_n\Lambda_l\cos(\beta_n - \beta_l + \Theta_n - \Theta_l) \tag{6}$$

Coupling term, $C_n = \Lambda_n * e^{(-i\beta_n)} * e^{(-i\Theta_n)}$ (7)

Where, Λ_n is the coupled fraction of the electric field, θ_m is the angular misalignment of the mirror, Θ_n is the Guoy phase shift, β_n is the phase shift for n reflections.

$$\Lambda_n = \frac{1}{\sqrt{1+n^2\overline{z}_m^2}}e^{-\frac{kz_R\left(1+5n^2\overline{z}_m^2\right)}{1+n^2\overline{z}_m^2}n^2\theta_m^2}$$
$$\Theta_n = -\tan^{-1}\left(n\overline{z}_m\right) + \frac{kz_R\left(3n\overline{z}_m - n^3\overline{z}_m^3\right)}{1+n^2\overline{z}_m^2}n^2\theta_m^2 \tag{8}$$
$$\beta_n = 2nk\overline{z}_m z_R$$

$k = \frac{2\pi n_c}{\lambda}$ is the wave vector for the refraction index of n_c

$\overline{z}_m = \frac{z}{z_R}$, where, $z_R = \sqrt{2}ks^2$ is the Rayleigh length for the beam of spot radius s

2.2. Sideband Evaluation Using Fourier series

When the two signals of different intensities (I_1 and I_2) interfere (this phenomenon will occur at the beam splitter of the Michelson interferometer shown in FIGURE 1 and in the Fabry- Perot cavity shown in FIGURE 5**Error! Reference source not found.**), the resulting intensity is given by,

$$\begin{aligned} I &= I_1 + I_2 + 2\sqrt{I_1 I_2}\,\sin\left((\phi) + \delta\sin\left(\omega_m t\right)\right) \\ &= I_1 + I_2 + 2\sqrt{I_1 I_2}\begin{bmatrix} \left(J_0\left(\delta\right) + 2\sum_{n=1}^{\infty} J_{2n}\left(\delta\right)\cos\left(2n\omega_m t\right)\right)\sin\left(\phi\right) + \\ \left(2\sum_{n=1}^{\infty} J_{2n-1}\left(\delta\right)\sin\left(\left(2n-1\right)\omega_m t\right)\right)\cos\left(\phi\right) \end{bmatrix} \end{aligned} \tag{9}$$

To form a quadrature signal, the carrier wavelength is modulated with a modulation depth (δ) and frequency (ω_m) which causes the phase shift (ϕ) of the harmonics.

The origin of the harmonics is given by from Jacobi-Anger expansion [9]. Since, it is a system of harmonically varying phase with harmonically varying input.

$$\begin{aligned} \cos\left(\delta\sin\left(\omega_m t\right)\right) &= J_0\left(\delta\right) + 2\sum_{n=1}^{\infty} J_{2n}\left(\delta\right)\cos\left(2n\omega_m t\right) \\ \sin\left(\delta\sin\left(\omega_m t\right)\right) &= 2\sum_{n=1}^{\infty} J_{2n-1}\left(\delta\right)\sin\left(\left(2n-1\right)\omega_m t\right) \\ \cos\left(\delta\cos\left(\omega_m t\right)\right) &= J_0\left(\delta\right) + 2\sum_{n=1}^{\infty}\left(-1\right)^n J_{2n}\left(\delta\right)\cos\left(2n\omega_m t\right) \\ \sin\left(\delta\cos\left(\omega_m t\right)\right) &= -2\sum_{n=1}^{\infty}\left(-1\right)^n J_{2n-1}\left(\delta\right)\cos\left(\left(2n-1\right)\omega_m t\right) \end{aligned} \tag{10}$$

$J_n\left(\delta\right) = \sum_{k=0}^{\infty}\frac{\left(-1\right)^k\left(\delta/2\right)^{2k+n}}{k!\left(k+n\right)!}$ is the Bessel function of order n

ϕ is the phase shift in the beams superposing

t is the time of modulation

From equation (9), for $n = 1$

$$I = I_1 + I_2 + 2\sqrt{I_1 I_2}\begin{bmatrix} \left(J_0\left(\delta\right) + 2J_2\left(\delta\right)\cos\left(2\omega_m t\right)\right)\sin\left(\phi\right) + \\ \left(2J_1\left(\delta\right)\sin\left(\omega_m t\right)\right)\cos\phi \end{bmatrix} \tag{11}$$

By using the Fourier series [10], the periodic signal $f(t)$ in the Fabry- Perot cavity can be represented by the sum of harmonics (summation in equation 9).

$$
\begin{aligned}
& f(t) = f(t+T) = \sum_{n=-\infty}^{\infty} c_n e^{j\omega_m nt} = c_0 + \sum_{n=-\infty}^{\infty} a_n \cos(n\omega_m t) + b_n \sin(n\omega_m t) \\
& \textit{because,} \\
& c_n = \frac{2}{T} \int_{-T/2}^{T/2} f(t) e^{j\omega_n x} dx \\
& \textit{where,} \\
& f(t) = R \\
& \omega_m = \frac{2\pi}{T} \\
& a_0 = \frac{2}{T} \int_0^T R dt \\
& a_n = \frac{2}{T} \int_0^T R \cos\left(n\omega_m t\right) dt \\
& b_n = \frac{2}{T} \int_0^T R \sin\left(n\omega_m t\right) dt
\end{aligned} \tag{12}
$$

The time waveform, $f(t)$ converges to form a periodic signals. Where, a_n is an even function and b_n is an odd function. The terms with $\cos\phi$ and $\sin\phi$ of the equation (11) is represented by a_n and b_n coefficients of equation (12).

FIGURE 7 shows the harmonics present in a signal. The magnitudes a_1 and b_1 representing the harmonics I_f and I_{2f} of the signal are plotted using the MATLAB code (see Appendix A) in section 2.5. These frequency values of the laser signal will be detected using the SR850 DSP lock-in amplifier (Section 3.1.3.9) and will be represented by the rotating vectors (Section 2.3).

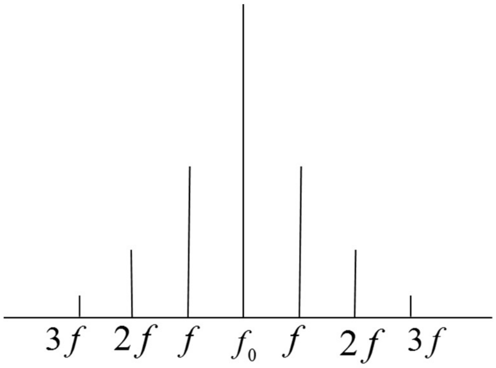

FIGURE 7: Sidebands of the signal

2.3. Rotating Vector Representation of Intensity

I_f and I_{2f} are the intensities at f and $2f$ frequencies, given by the magnitudes of the Fourier coefficients, a_1 and b_1. The phase shift in the signal, (see FIGURE 8).

$$\phi = \tan^{-1}\left(\frac{I_{2f}}{I_f}\right)$$

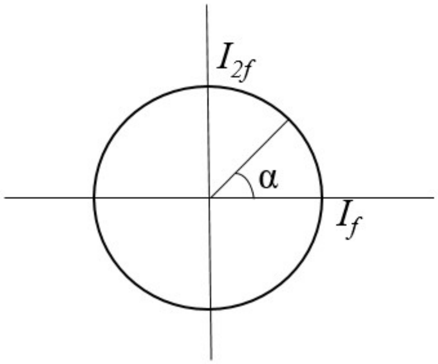

FIGURE 8: Rotating vector representation of intensity of *f* and *2f* signals

From the phase shift, the displacement, $\Delta h = \frac{\lambda}{2}\left(\frac{\phi}{360} + n\right)$ can be calculated. Where, n is the number of times the vector completes its full rotation, which is the equal to number of complete fringes (m) produced during the displacement (will be sensed by the photodetector).

2.4. Fourier Coefficients of Intensity in the Fabry- Perot cavity- MATLAB

The theoretical model used the equations of Wilkinson et. al. [1], shown below, to find the two frequencies the laser light is modulating. (f and $2f$) Following paragraphs explains the structure of the Matlab code (Appendix A) used.

In the main function ReflFourierCoeffvaryingLambda.m, Cavity separation (Δz) of length 5 μm ranging from 150 μm to 155 μm is analyzed. The laser signal with spot radius, s of 3.7 μm is modulated with a modulation depth, δ of 20 nm and frequency, f_m = 1200 Hz in the presence of air $(n_c = 1)$. Mirror reflectivity (of the target), $r_m = 0.2$ is chosen, because the reflectivity of single mode glass fiber is around 0.2, which will help in better coupling of light back in to the fiber from the target. t is the time increment and $T = \frac{1}{f_m}$.

In the function FPfiberfuncRmvaryinglambdaKA.m, the modulated wavelength, $\lambda = \lambda_0 + \Delta\lambda$ (where, λ_0 is 1550 nm and $\Delta\lambda$ is $\delta \sin \omega_m t$) varies the Wave vector, $k = 2\pi n_c / (\lambda + \Delta\lambda)$ and the fraction $\bar{z}_m = z / z_R$. This in turn varies the coefficients in equation (8) in the sub function Ccoeffsm.m.

An array of intensity (R) (equation (6)) is generated for the co-efficient values in the function Rarraycreator.m. The simulation is conducted for N = 5 reflections as the reflectivity reduces rapidly as the number of reflections increases. The intensity is used to find the Fourier coefficients a_1 and b_1 representing f and $2f$ harmonics in the main function ReflFourierCoeffvaryingLambda.m.

2.5. MATLAB Simulation Results

2.5.1. Larger Modulation Depth and Separation

FIGURE 9 plots the intensity that is shown to decrease with increasing separation (over a translation of $\Delta z = 50$ μm) of the mirror from fiber end. Since, the increase in z component in the equation (7) reduces the coupling coefficient C_n. For a frequency modulation depth, δ of 20 nm, FIGURE 10 shows the variation of the numerically calculated Fourier coefficients, a_1 and b_1 with the separation.

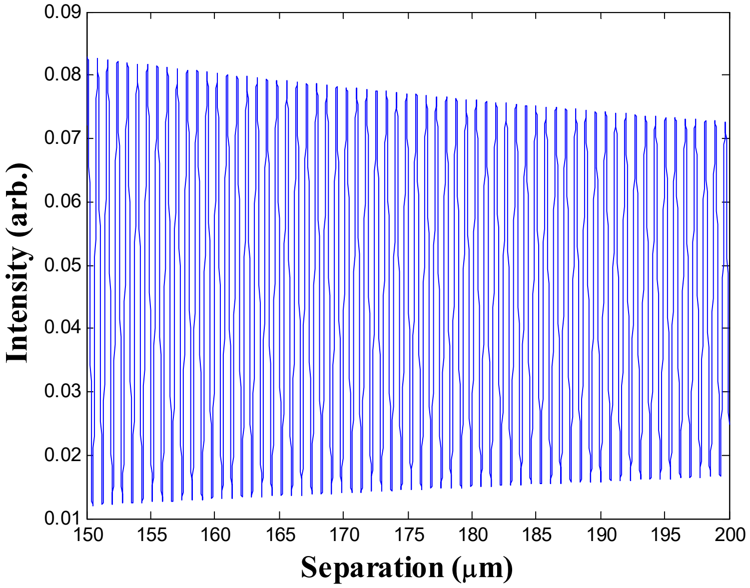

FIGURE 9: Reflectivity with separation (Δz = 50 μm, δ = 20 nm)

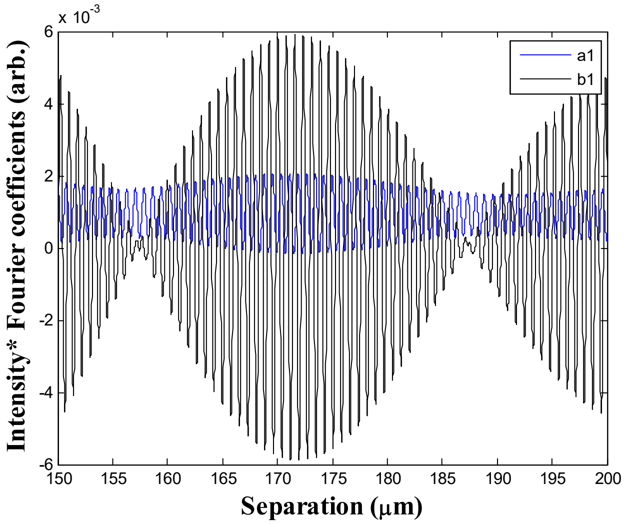

FIGURE 10: Fourier coefficients with separation Δz = 50 μm

2.5.2. Smaller Modulation Depth and Separation

The following simulation results are for a change in separation of Δz = 5 μm and a modulation depth of δ = 0.05 nm. Modulating wavelength is shown in FIGURE 11, FIGURE 12 shows that intensity decreases with respect to the separation (Δz), and FIGURE 13 shows the variation of Fourier coefficients, a_1 and b_1 with separation.

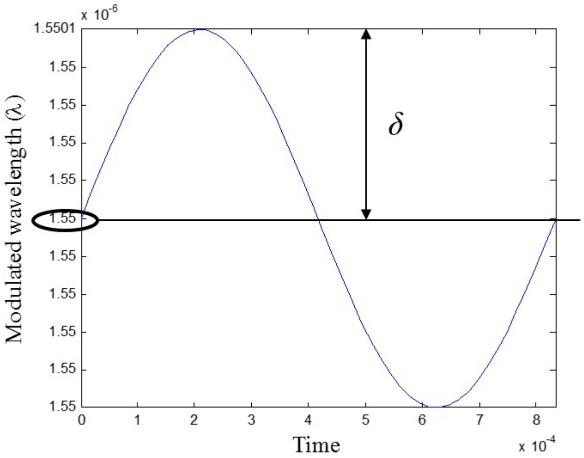

FIGURE 11: Modulated wavelength (λ_0 = 1550 nm, δ = 0.05 nm)

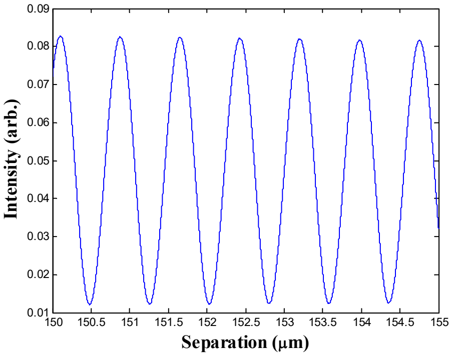

FIGURE 12: Reflectivity with separation ($\Delta z = 5$ µm, δ = 0.05 nm)

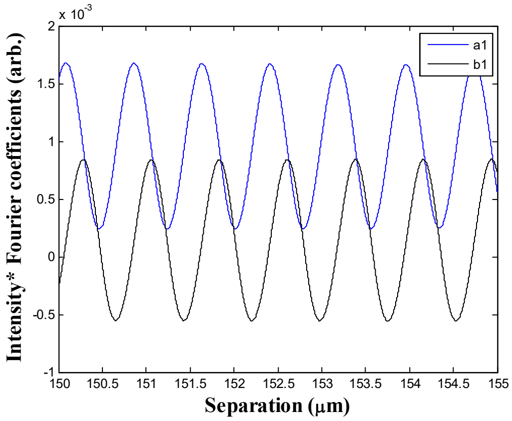

FIGURE 13: Fourier coefficients with separation $\Delta z = 5$ µm

2.5.3. Rotating Vector Representation of Intensity- MATLAB simulation

At the translation of $\Delta z = 5$ µm and with a modulation depth of 0.05 nm, the rotating vector of the magnitude f and $2f$ signals is plotted. A shape (FIGURE 14) resembling the circle shown in FIGURE 8 is achieved. It's three dimensional plot is shown in FIGURE 15.

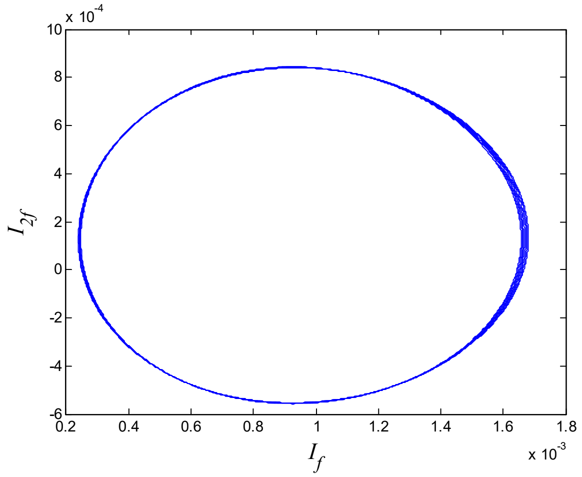

FIGURE 14: Rotating vector (Δz =5 µm, δ = 0.05 nm)

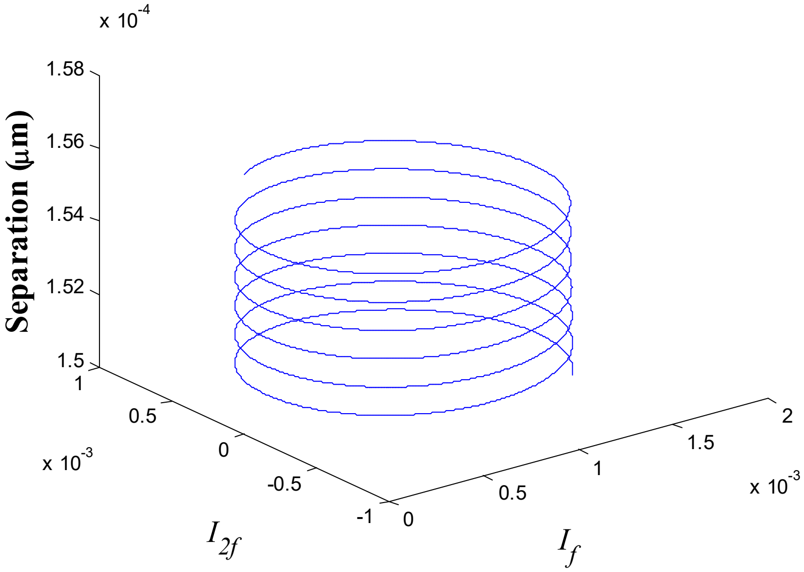

FIGURE 15: Rotating vector in three dimensional plot (Δz = 5 µm, δ = 0.05 nm)

For the modulation depth of 1 nm, with separation at Δz = 5 µm, the rotating vector got shrink and resembled an ellipse (FIGURE 16).

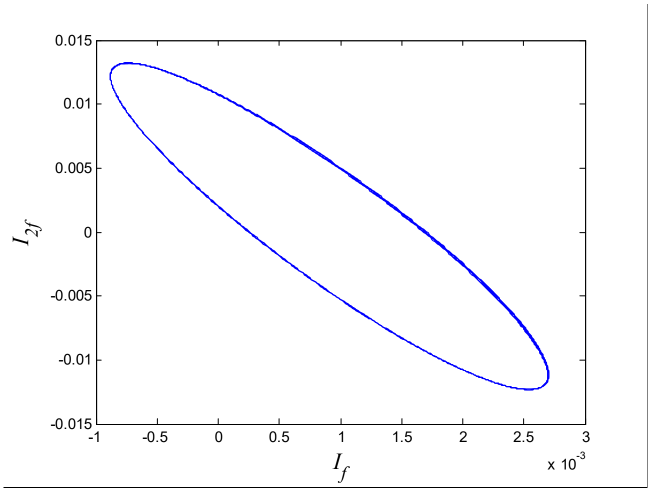

FIGURE 16: Rotating vector (Δz= 5 µm, δ = 1 nm)

In FIGURE 17, even though path traced looks similar to FIGURE 14, the deviation in the path traced got larger as the separation is increased to Δz = 10 µm with a modulation depth of 0.05 nm.

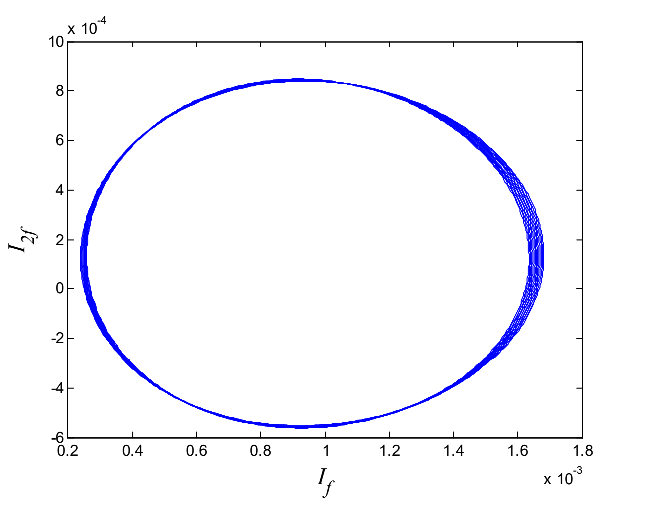

FIGURE 17: Rotating vector (Δz= 10 µm, δ = 0.05 nm)

The deviation got much larger as the separation is increased to 50 µm (FIGURE 18) with the modulation depth of 0.05 nm.

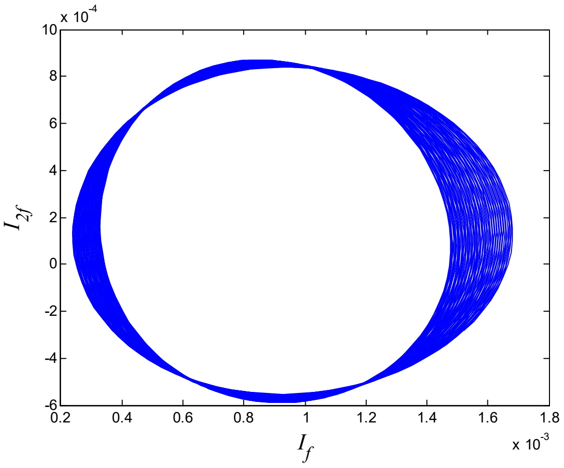

FIGURE 18: Rotating vector (Δz = 50 µm, δ = 0.05 nm)

CHAPTER 3: EXPERIMENTAL STUDY

3.1. Process Development and Performance Studies

3.1.1. Diode Driver

The goal of the diode driver is to provide a controllable current through the laser diode. The principle is that the temperature of the laser crystal varies as the current is varied, and this can be used to achieve wavelength modulation. The circuit of the laser diode driver with modulating current input is shown in FIGURE 19. The laser's (VLM-635-03 LPA) operating current is 40±15 mA (which is always positive, i.e. varying from 25 mA to 55 mA). Therefore, an offset is created to the sine input to op-Amp OPA137 (2).

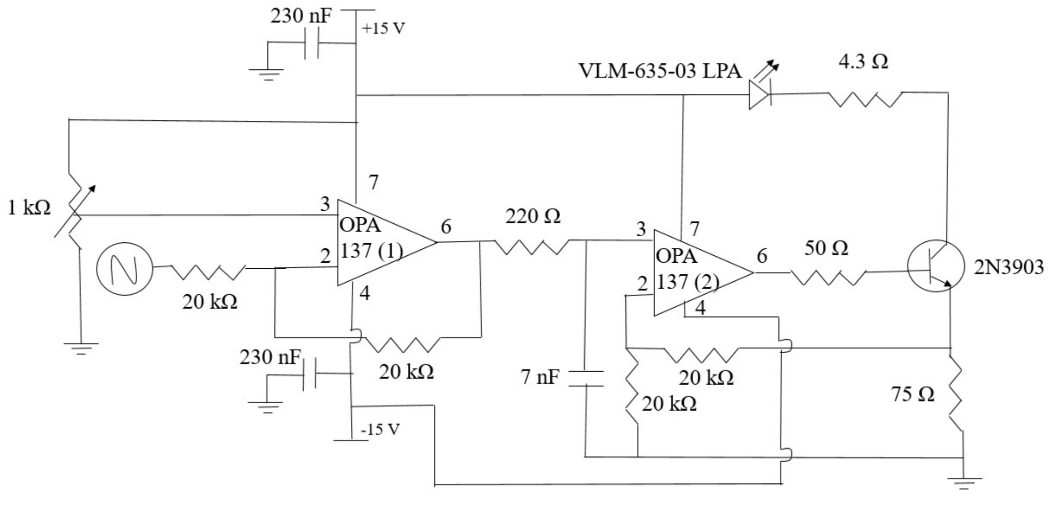

FIGURE 19: Circuit of the laser driver

A Multisim™ model (FIGURE 20) of the circuit is created. It consists of two stages. Stage 1: To produce a voltage out with an offset of 3 V. An inverting amplifier (OPA137) produces an inverted voltage signal with an offset. The offset is achieved using potentiometer of 1 kΩ. The output from stage1 is given as the input to the 2nd stage through a low pass filter of cut-off frequency 100 kHz.

Stage 2: includes a non-inverting amplifier (OP07) with a gain of 2 (the output voltage produced is twice the amplitude of the signal given in (FIGURE 21)). A bi-polar transistor of npn-type (2N 3903) is used to drive the current through the laser diode. The voltage going to pin 2 is equal to half the voltage through feedback resistor of 75 Ω. (we have used a resistor of 4.3 Ω load to represent the laser diode).

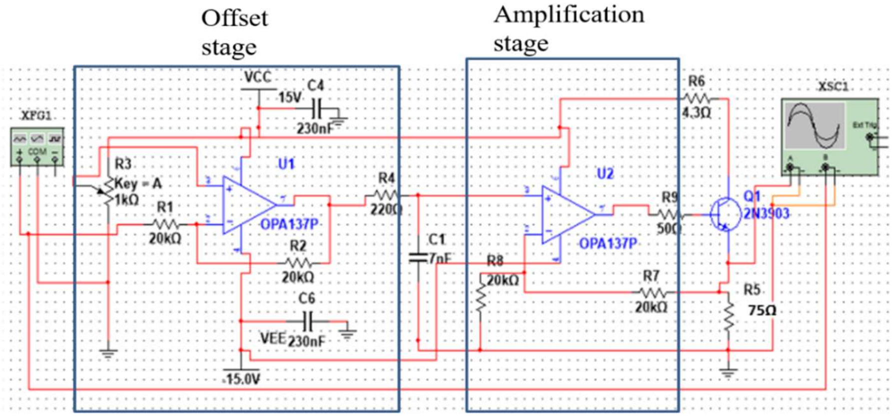

FIGURE 20: Multisim™ simulation model of laser driver

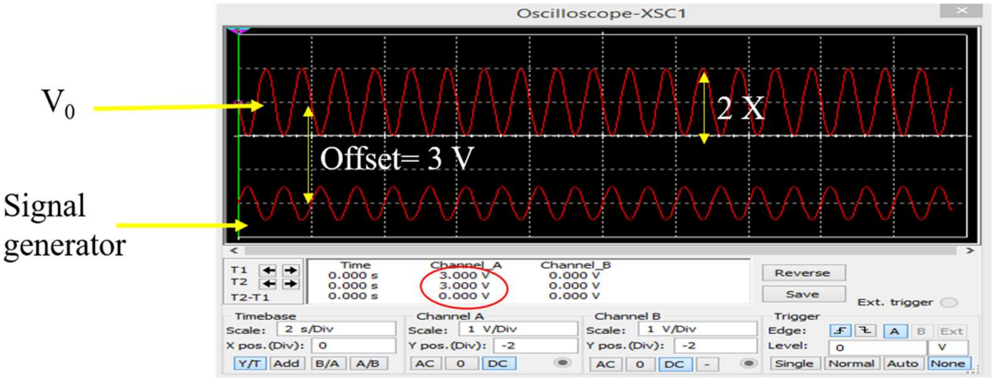

	Time	Channel_A	Channel_B
T1	0.000 s	3.000 V	0.000 V
T2	0.000 s	3.000 V	0.000 V
T2-T1	0.000 s	0.000 V	0.000 V

Timebase
Scale: 2 s/Div
X pos.(Div): 0
Y/T Add B/A A/B

Channel A
Scale: 1 V/Div
Y pos.(Div): -2
AC 0 DC

Channel B
Scale: 1 V/Div
Y pos.(Div): -2
AC 0 DC -

Trigger
Edge: A B Ext
Level: 0 V
Single Normal Auto None

FIGURE 21 Multisim™ simulation- output signal of the laser driver

FIGURE 21 shows that signal in the top is amplified twice and has an offset of 3 V from the signal produced using the signal generator shown in bottom.

3.1.1.1 Performance study of the Diode driver

Without the laser being connected, the maximum offset voltage achieved using the potentiometer is 11.56 V (In FIGURE 22, the scale is adjusted to 9.56 divisions and the output is still offset by 2 V, which makes the total offset 11.56 V). Therefore the maximum current that can be driven is V/R = 11.56 V/75 Ω = 154.13 mA (FIGURE 22).

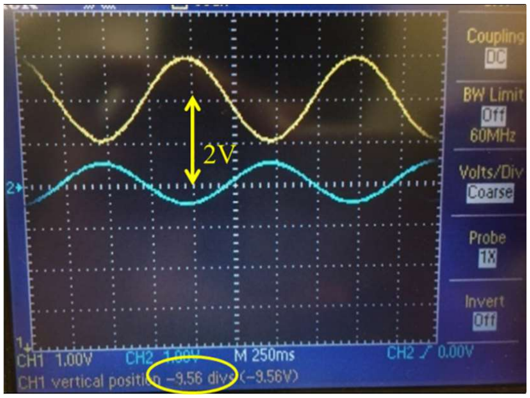

FIGURE 22: Offset signal

Based on the manufacturers data sheet (see Appendix B), the laser used (VLM-635-03 LPA) requires an operating current range of 40±15 mA. As the circuit at the transistor has a resistance of 75 Ω, voltage for the maximum current (55 mA) that can drive the laser is, IR= 55 mA x75 Ω = 4.125 V.

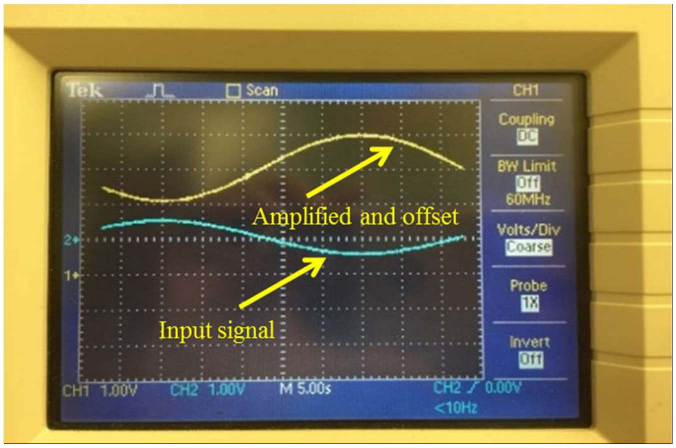

FIGURE 23: modulating signal input

If the offset of 3 V is provided using the potentiometer and the amplifier has a gain of 2 (FIGURE 23), the maximum amplitude of modulating signal is calculated as 4.125 - 3= 1.125 V and 1.125/2= 0.5625 V (divided by 2, as the final output will have a gain of 2). The fabricated circuit of the laser driver with components are shown in FIGURE 24.

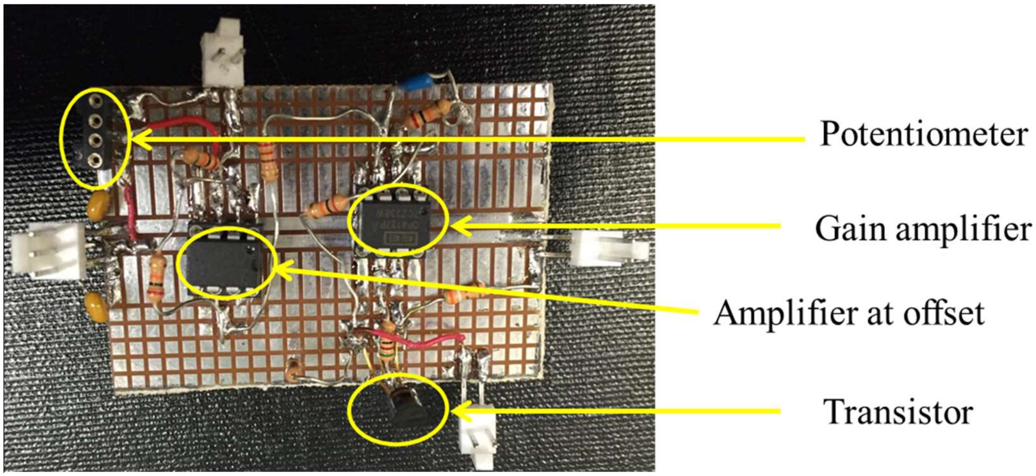

FIGURE 24: Fabricated circuit- laser driver

3.1.2. Photodetector

The photodetector circuit show in FIGURE 25 is configured as a trans-impedance amplifier and has a switchable resistor ranging 62 KΩ to 2 MΩ to change the sensitivity of photodetector.

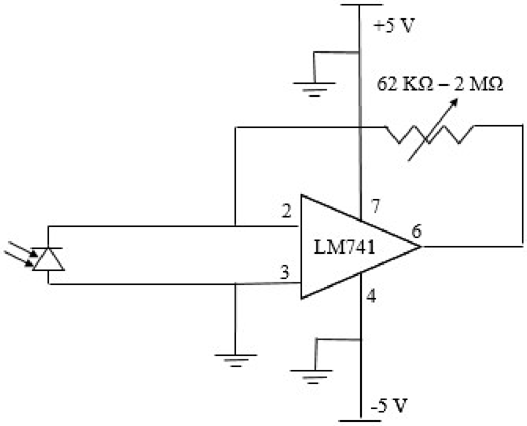

FIGURE 25: Circuit- Photodetector

A Multisim™ simulation (FIGURE 26) is conducted for the photodetector circuit. An oscillating current source is used, since a photodiode model is not available with our current installation of Multisim™.

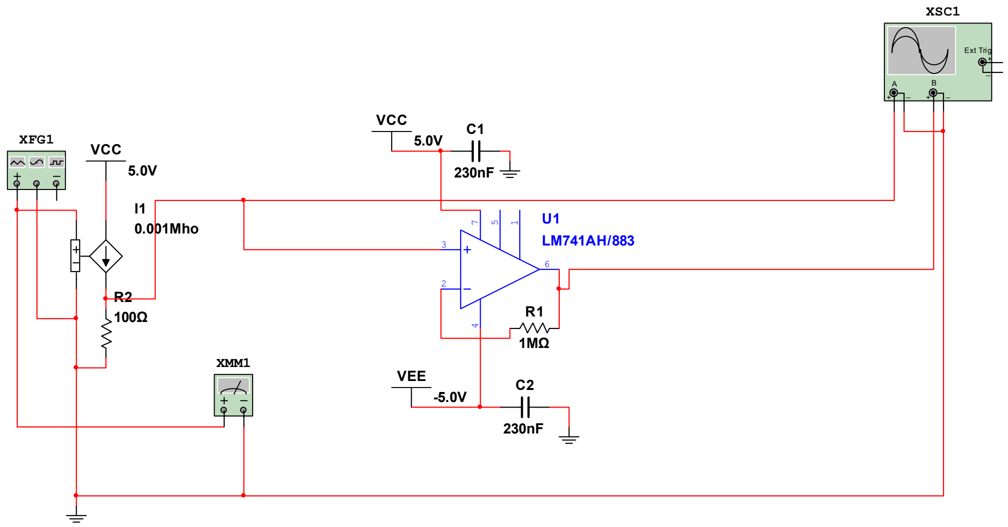

FIGURE 26: Multisim model- Photodetector circuit

Multisim™ simulation results (FIGURE 27) shows that the output is a direct representation of the sinusoidal wave sent using the signal generator. Thus the circuit can produce an output proportional to the change in intensity at the photodetector. And the actual photodetector built is shown in FIGURE 28.

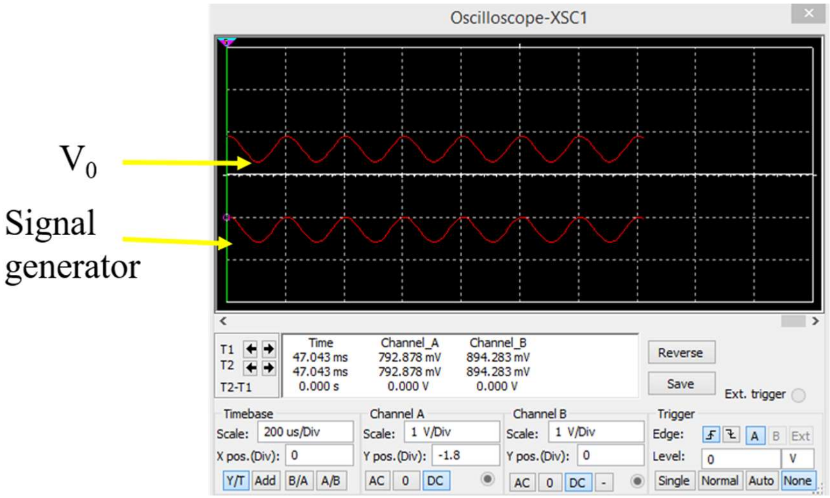

	Time	Channel_A	Channel_B
T1	47.043 ms	792.878 mV	894.283 mV
T2	47.043 ms	792.878 mV	894.283 mV
T2-T1	0.000 s	0.000 V	0.000 V

Timebase
Scale: 200 us/Div
X pos.(Div): 0

Channel A
Scale: 1 V/Div
Y pos.(Div): -1.8

Channel B
Scale: 1 V/Div
Y pos.(Div): 0

Trigger
Edge: A
Level: 0 V

FIGURE 27: Multisim simulation- Photo detector

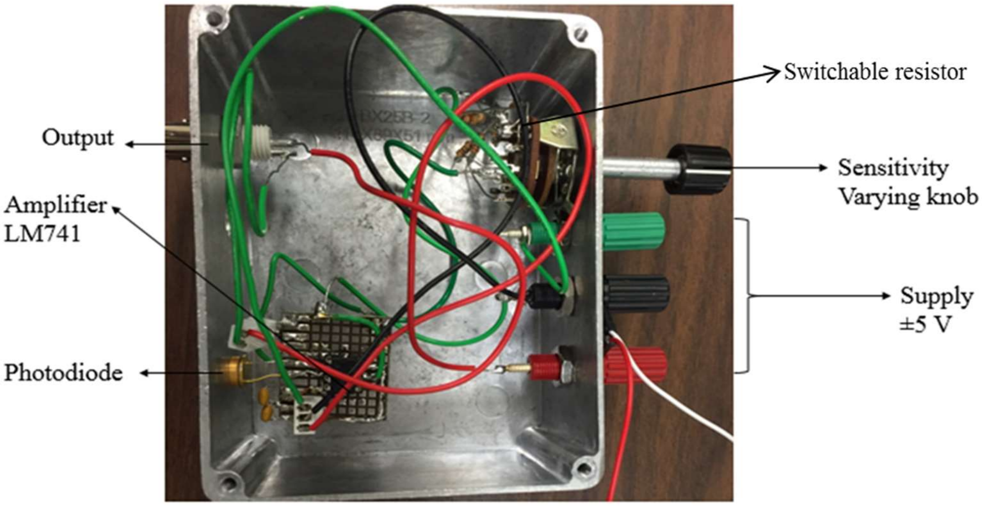

FIGURE 28: Photodetector circuit with the switchable resistor

3.1.3. Michelson Interferometer

3.1.3.1. Experimental Setup

The Michelson interferometer is setup on an optical table with a photograph of the set-up is shown in FIGURE 29. The laser source used is a Red laser diode VLM-635-03 LPT with a peak emission wavelength of 630 ~ 645 nm. The modulated beam from the laser diode is focused to a beam splitter. Its *x*, *y* and *z* axis can be adjusted using the stage (Nanomax-TS) shown in FIGURE 30.

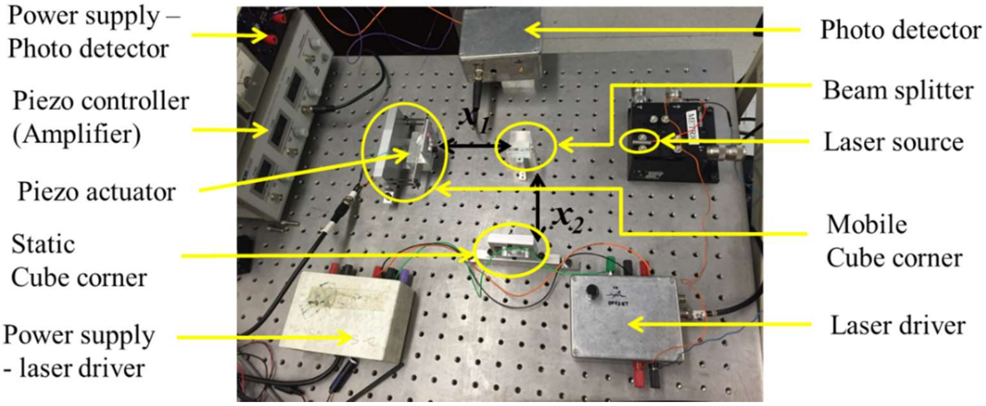

FIGURE 29: Michelson interferometer setup

The laser beam from the diode enters the beam splitter and splits in two. One enters a static cube corner (shown in FIGURE 31), mounted to a setup which is adjustable in *y* and *z* directions. This helps the beam from the beam splitter to enter the cube corner. The second beam from the splitter enters a cube corner that is is mounted on a flexure guided translation stage, FIGURE 32 and FIGURE 33.

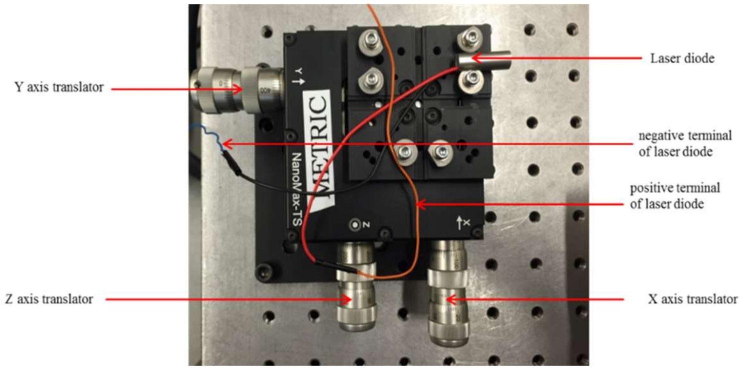

FIGURE 30: Laser stage with translation direction control

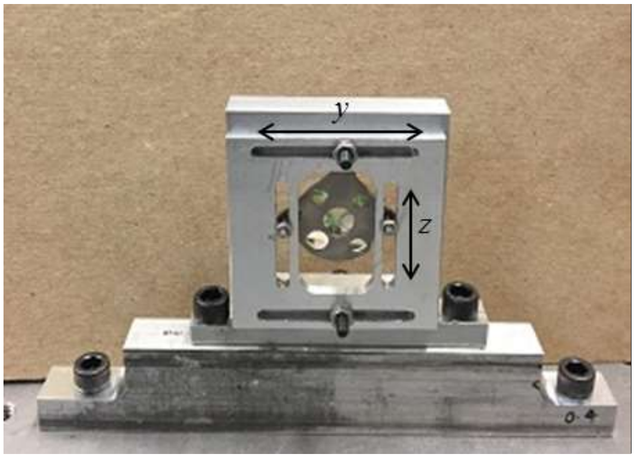

FIGURE 31: Static cube corner, arrows indicate adjustment freedoms

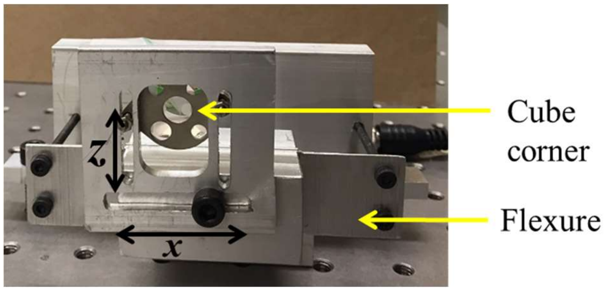

FIGURE 32: Mobile cube corner, arrows indicate adjustment freedoms

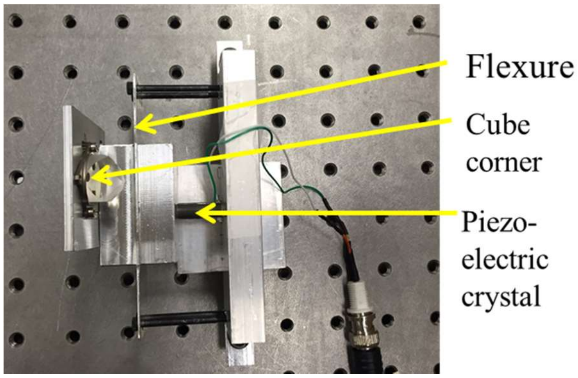

FIGURE 33: Mobile cube corner showing piezo

The piezo electric crystal is actuated by Thorlabs 3-axis Piezo controller MDT693A that provides an amplification of 15 to a voltage applied to its input using a DAC (NI-DAQ SCB-68) with software developed using LabVIEW (FIGURE C.1 and

C.2). The cube corner can also be adjusted align the beam from the beam splitter to enter the cube corner and return to the detector (*y*, *z* and *x*, *z* shown in FIGURE 31 and FIGURE 32 respectively)

The beams reflected from the cube corners return to the beam splitter, and overlap at the photodetector. The photodetector senses the change in intensity of the beam as the path length varies. The optical path difference of the travelled beam is $2x$, therefore, displacement of the moving mirror, $x = m\frac{\lambda}{2}$. (13)

m is the number of fringes observed.

3.1.3.2. Control and Measurement

A flow diagram of the complete setup is shown in FIGURE 34. The piezo electric crystal of the mobile cube corner is actuated by the Piezo controller which is, in turn, controlled by the Ramp signal generated using the LabVIEW program. This program runs together with another real time Data acquisition program (FIGURE C.1 and FIGURE C.2 in Appendix C). Interference between the beams as the cube corner displaces is detected by the photo detector (PD) and measured using NI-DAQ that also measures the demodulated outputs from two Lock-in amplifiers (denoted A and B). The lock-in amplifier B is phase-locked with the sine wave Reference from A. A problem occurred due to the low voltage amplitude necessary for the diode modulation circuit that was too small for locking the second lock-in B. To overcome this issue, a large modulating voltage from the lock-in A is used for phase locking and also fed to the laser driver through NI- DAQ. This program then reads the voltage and immediately sends this as an output from NI- DAQ at 1/10 of the voltage from the Lock-in A enabling control of the driver from the instrumentation computer.

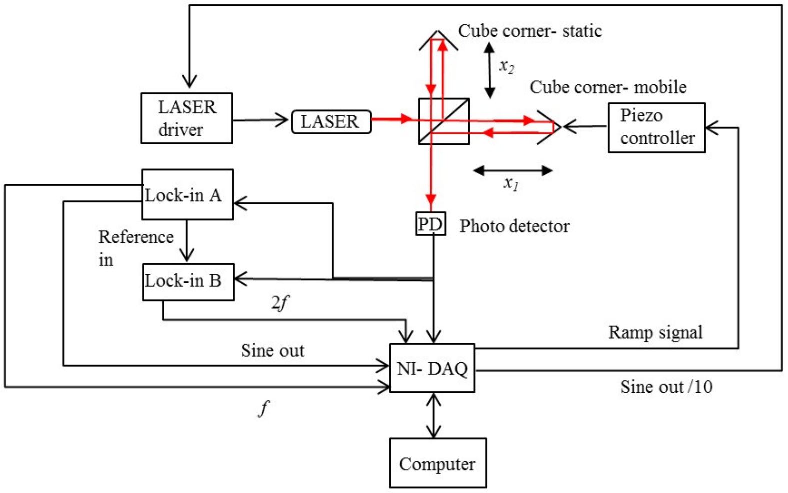

FIGURE 34: Flow diagram- Control and measurement of displacement and harmonics

The front panel of the LabVIEW program is shown in FIGURE 35. Using this program, the user can observe the Ramp signal to the piezo controller (amplified 15 times), intensity measured using the photodetector, f and $2f$ harmonics of the measured signal and their x-y plot. FIGURE 36 shows the Lock-in amplifiers used.

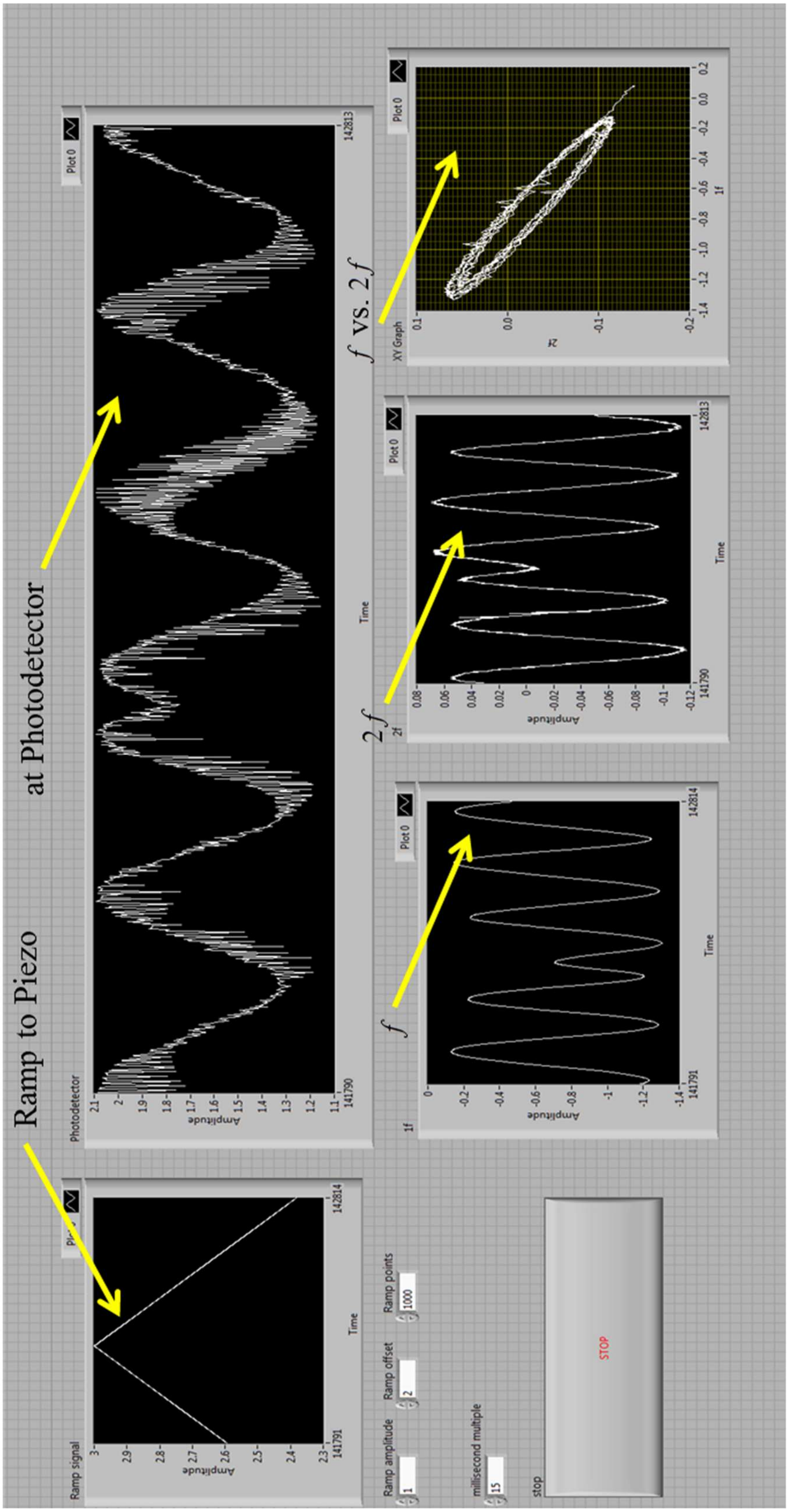

Ramp to Piezo

at Photodetector

f

2*f*

f vs. 2*f*

Ramp amplitude 1

Ramp offset 2

Ramp points 1000

millisecond multiple 15

stop

FIGURE 35: Front panel of the LabVIEW program

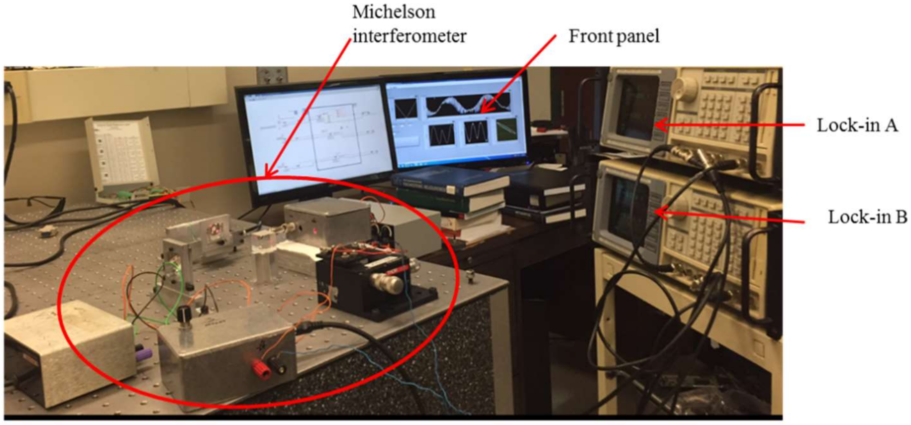

FIGURE 36: Experimental setup showing Lock-in amplifiers

Tests in the following sections 3.1.3.3 to 3.1.3.6 are conducted with an unmodulated laser. The laser driver (FIGURE 19) is offset to its operation range by using the potentiometer alone, and it does not have a modulating current input. The flow diagram of the setup is shown in FIGURE 37. The displacements are achieved using the ramp signal generated using the LabVIEW program (for FIGURE 38 to FIGURE 59) sent to the piezoelectric amplifier (piezo controller with a gain of 15), and the piezoelectric amplifier actuates the piezo electric crystal of the mobile cube corner. The actuation of piezo electric crystal displaces the cube corner. The interference between the beams as the cube corner displaces is detected by the photo detector (PD) and measured using NI-DAQ. The setup does not include the Lock-in amplifiers shown in the previous flow diagram (FIGURE 34), as these experiments do not involve the sensing of f and $2f$ harmonics.

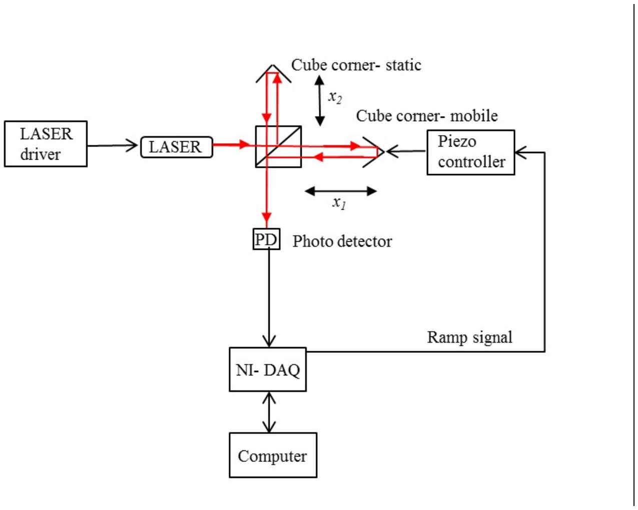

FIGURE 37: Flow diagram- Control and measurement of displacement

3.1.3.3. Calibration

The interferometer was calibrated with the Lion precision capacitance gauge having a sensitivity of 0.4 V/µm. Displacement of the cube corner (achieved by the ramp signal) is measured using the capacitance displacement sensor (FIGURE 38). The capacitance sensor results and the intensity response of the photo detector using the Michelson interferometer are compared in FIGURE 39.

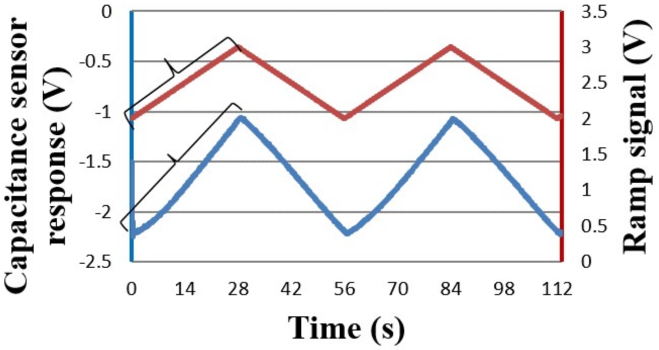

FIGURE 38: Calibration using capacitance displacement sensor

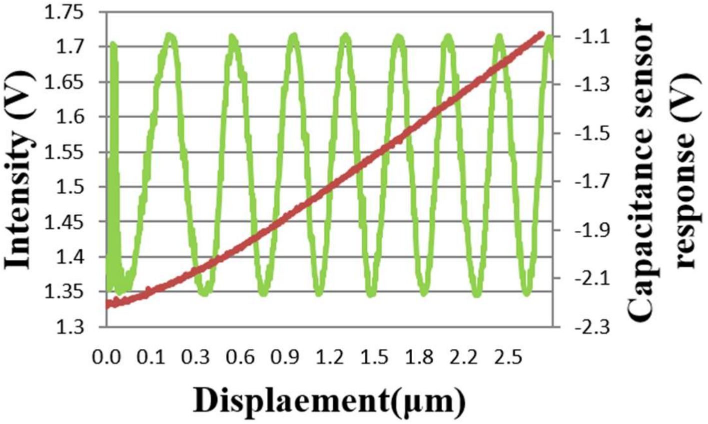

FIGURE 39: Photodetector measured intensity and the capacitance displacement sensor response

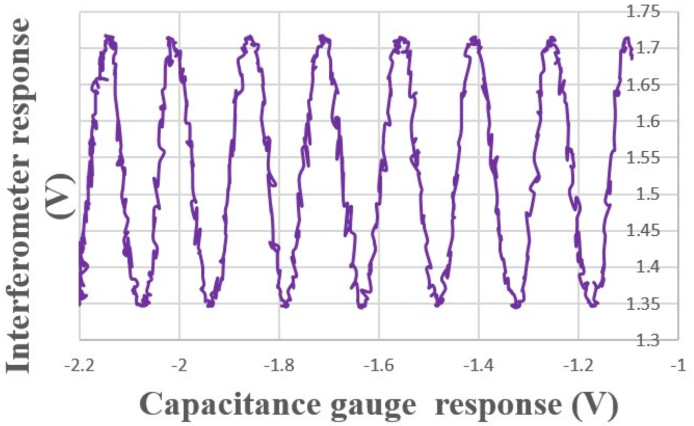

FIGURE 40: Capacitance displacement sensor vs. Michelson interferometer

The displacement is measured by the Michelson interferometer using the wavelength of intensity response curve (FIGURE 1). Each period of it corresponds to half of the wavelength of the laser signal. The displacement with respect to the increasing ramp signal (shown in curly braces in FIGURE 38) is measured as 2.54 µm by the interferometer, (since m= 8 and λ = 635 nm, please see equation (13)). And the displacement measured by the capacitance sensor (FIGURE 38) is 2.7 µm. The difference between their values is 160 nm (2.7 µm - 2.54 µm). The fringes observed using the interferometer and the capacitance sensor result are plotted to see the linearity among them (FIGURE 40).

The non-linear expansion and contraction of the Piezo electric crystal is demonstrated using the hysteresis curve (FIGURE 41).

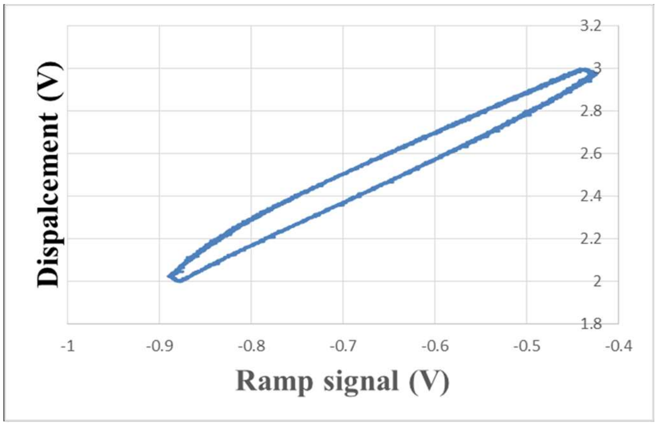

FIGURE 41: Hysteresis of piezoelectric crystal's displacement

3.1.3.4. Tests with varying displacements

Following plots (FIGURE 42 to FIGURE 49) show the intensity response of the photodetector with respect to varying ramp amplitude (varying displacement of cube corner).

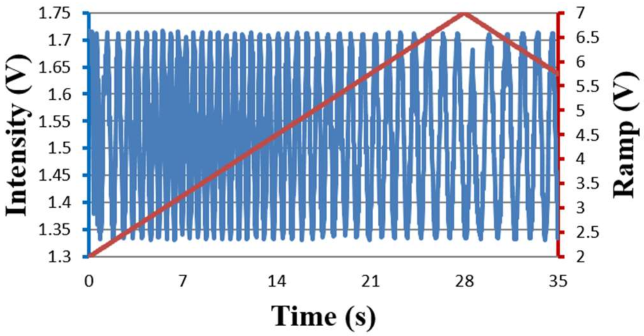

FIGURE 42: Intensity with ramp amplitude at 5 V

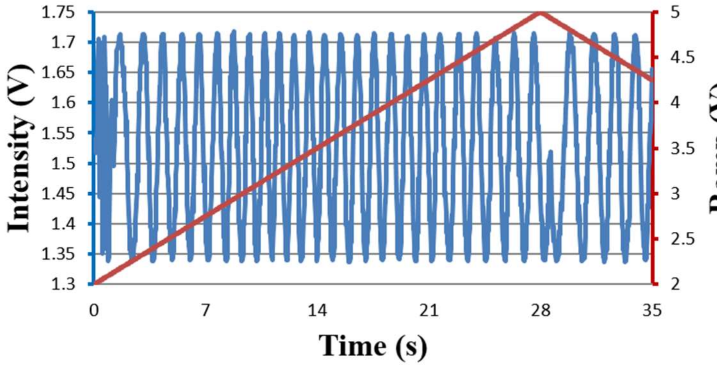

FIGURE 43: Intensity with ramp amplitude at 3 V

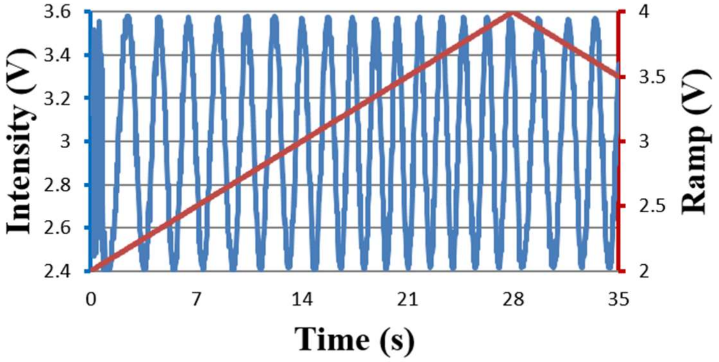

FIGURE 44: Intensity with ramp amplitude at 2 V

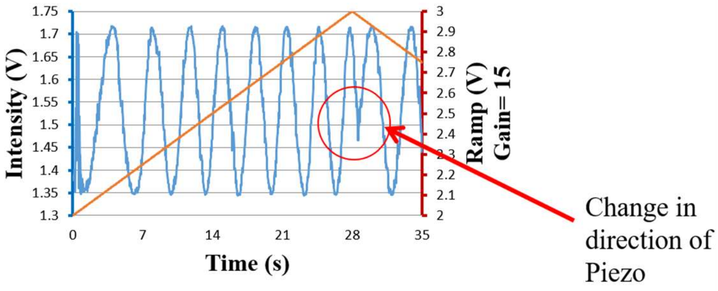

Change in direction of Piezo

FIGURE 45: Intensity with ramp amplitude at 1 V

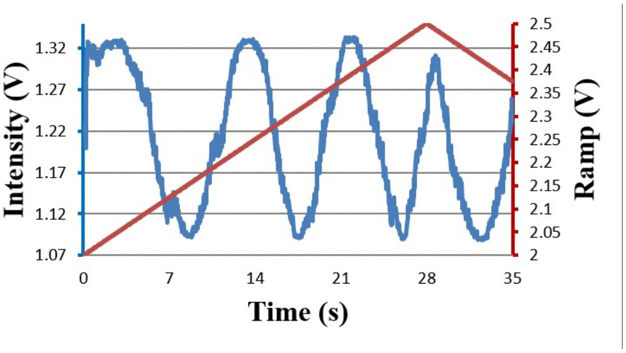

FIGURE 46: Intensity with ramp amplitude at 0.5 V

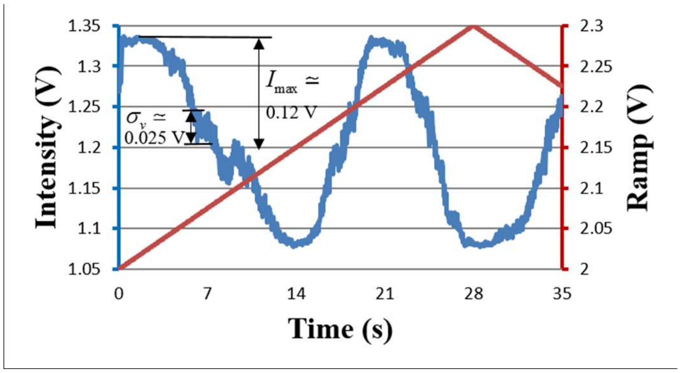

FIGURE 47: Intensity with ramp amplitude at 0.3 V

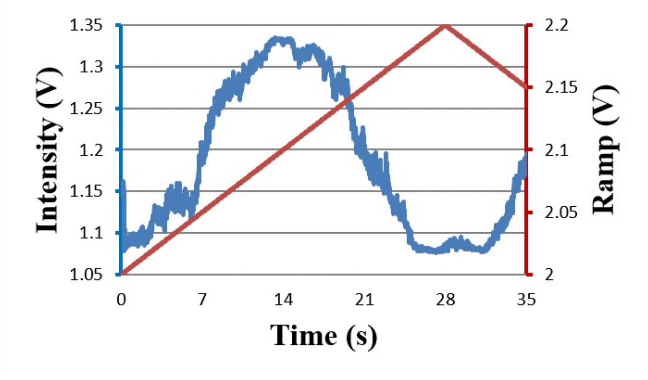

FIGURE 48: Intensity with ramp amplitude at 0.2 V

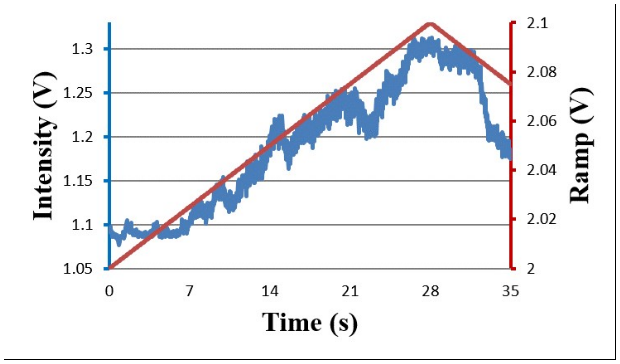

FIGURE 49: Intensity with ramp amplitude at 0.1 V

In FIGURE 45, a blip is observed when the direction of the piezo electric crystal reverses.

The resolution of the Michelson interferometer set up is calculated using FIGURE 47,

$$
\begin{aligned}
&\phi = \frac{4\pi x}{\lambda} \\
&\sigma_\phi = \frac{\sigma_v}{I_{\max}} = \frac{4\pi\sigma_x}{\lambda} \qquad (14) \\
&\sigma_x = \frac{\lambda\sigma_v}{4\pi I_{\max}}
\end{aligned}
$$

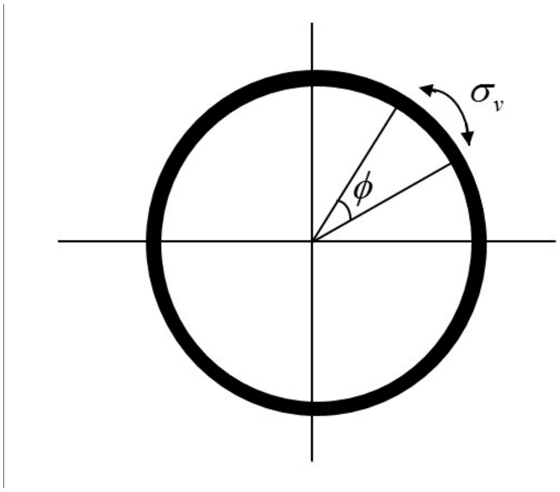

FIGURE 50: Rotating vector representing noise in the signal

Where,

ϕ is the phase of the signal

x is the displacement

σ_ϕ is the standard deviation of phase

σ_v = 0.025 V is the amplitude of noise in the signal

$I_{\max}$ = 0.12 V is the maximum intensity of the signal

λ = 635 nm is the wavelength of the light used

Thus, the resolution of the system σ_x is calculated as 10.533 nm.

3.1.3.5. Tests with varying displacement rate

Following plots (FIGURE 51 to FIGURE 54) shows the intensity response of the photodetector with the ramp amplitude of 1 V (displacement of 2.54 µm) at varying rate.

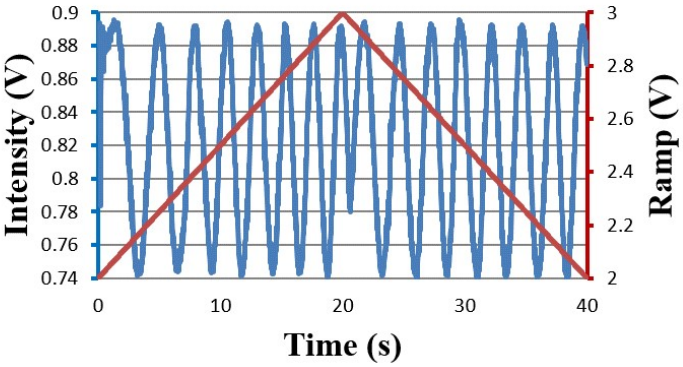

FIGURE 51: Intensity with ramp amplitude of 1 V in 20 s

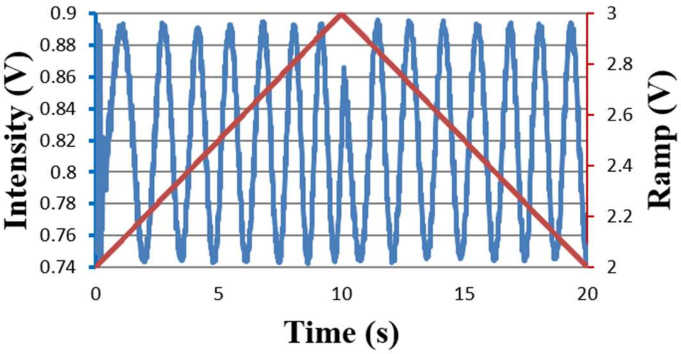

FIGURE 52: Intensity with ramp amplitude of 1 V in 10 s

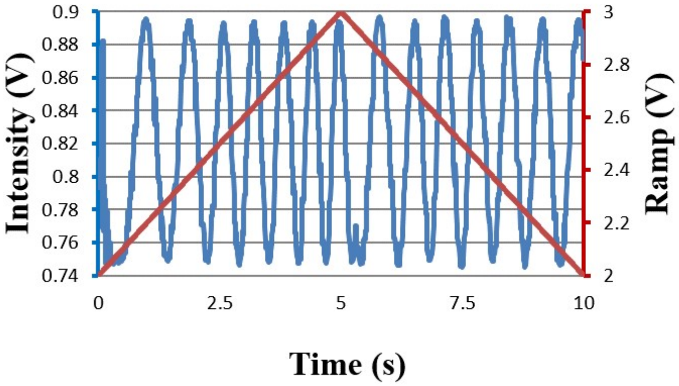

FIGURE 53: Intensity with ramp amplitude of 1 V in 5 s

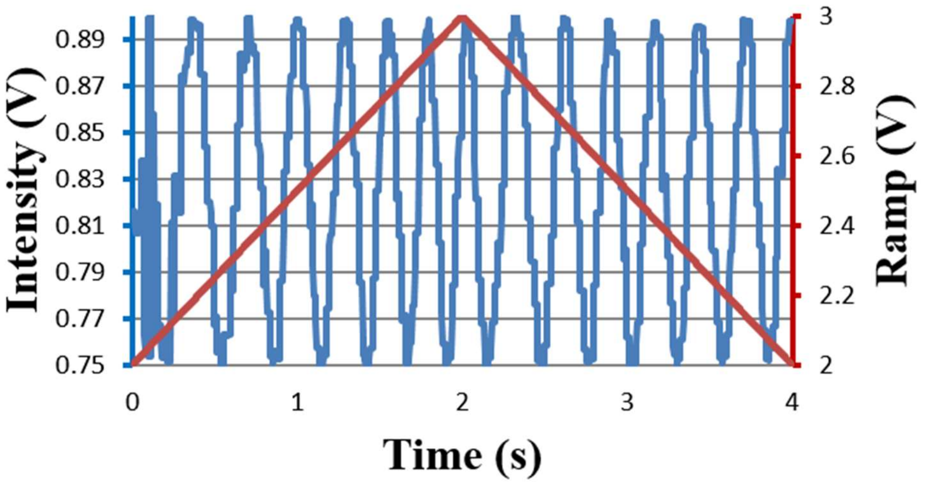

FIGURE 54: Intensity with ramp amplitude of 1 V in 2 s (Digitized)

We observed that the signal starts to digitize (FIGURE 54), since the sampling rate that the My- DAQ was set was lower than the rate we tried to measure.

3.1.3.6. Coherence length

Coherence length is defined as the maximum length up to which fringes will be visible. Following plots are used to find a conservative estimate of the coherence length of the laser. The distance (x_2) (FIGURE 34) between the beam splitter and the static cube corner is varied for the experiments, and the mobile cube corner is displaced using the ramp signal. The curves looked clear until the difference $(x_2 - x_1)$ was 0.253 m (FIGURE 57), after which the fringes became distorted (FIGURE 58), and the visibility was $V = \frac{I_{\max} - I_{\min}}{I_{\max} + I_{\min}} = \frac{1.45 - 0.75}{1.45 + 0.75} = 0.318$.

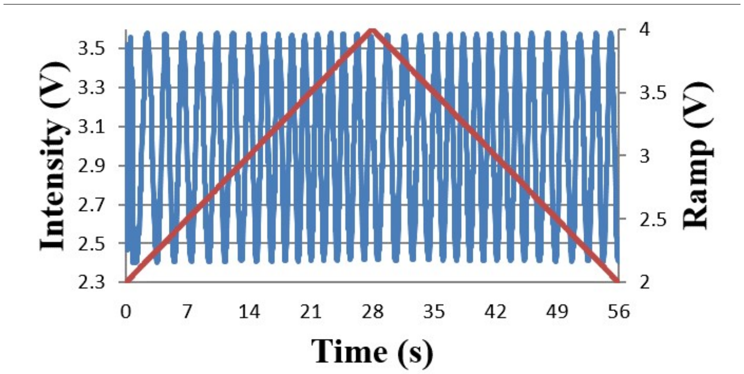

FIGURE 55: Intensity with cube corners at $(x_2 - x_1)$ = 0 m with ramp signal indicating value input to the piezoelectric amplifier

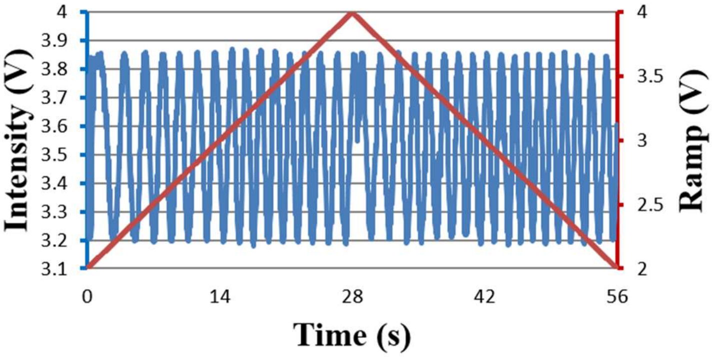

FIGURE 56: Intensity with cube corners at $(x_2 - x_1)$ = 0.127 m

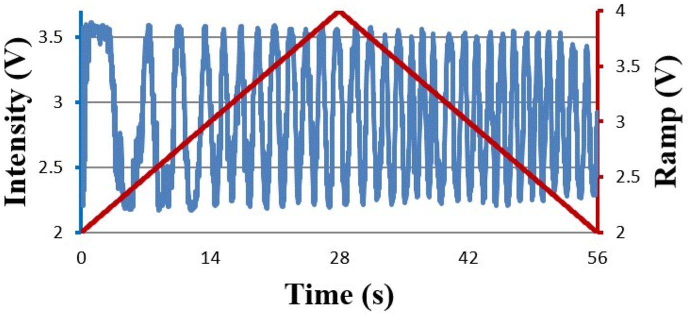

FIGURE 57: Intensity with cube corners at $(x_2 - x_1)$ = 0.253 m

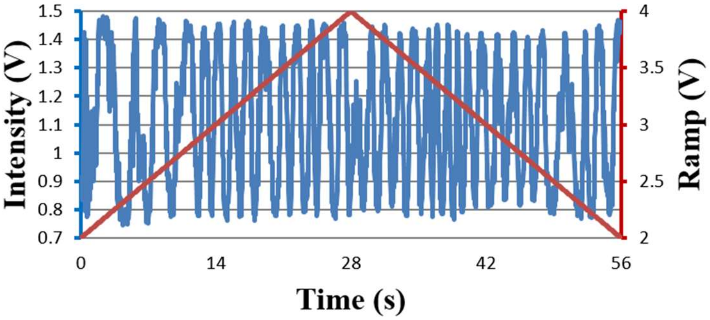

FIGURE 58: Intensity with cube corners at $(x_2 - x_1)$ = 0.383 m

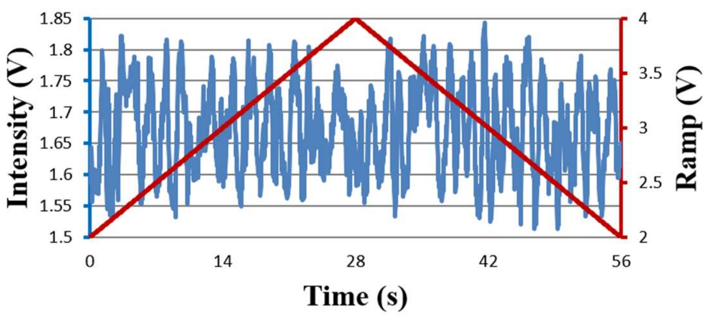

FIGURE 59: Intensity with cube corners at $(x_2 - x_1)$ = 0.635 m

Coherence length is also defined as the distance at which the intensity of the beam drops $1/e$ of its peak intensity I_0. We have considered only one half of the curve ($\Delta\lambda$) (FIGURE 60) for the experiments, consideration of the other half gives us a multiple of 2. And also, the beam travels the distance $(x_2 - x_1)$ twice (travelling to the cube corner and reflects back), we get another multiple of 2. Thus, an estimate of the smallest coherence length will be around 4 times this value ($4 \times 0.253 = 1.012$ m). Other issues that lead to the reduction in intensity at the photodetector are divergence and alignment of the beam.

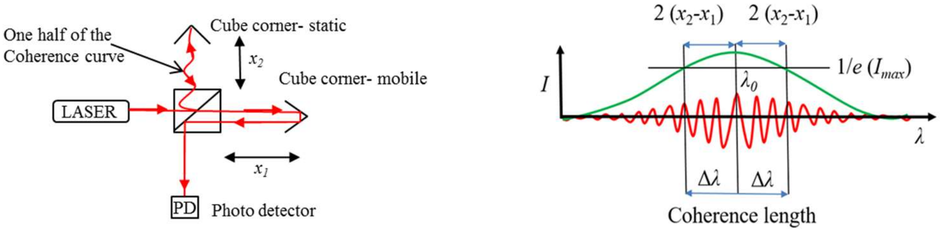

FIGURE 60: Coherence length curve

3.1.3.7. Measurement of modulating wavelength

The amount of wavelength modulation achieved in the laser beam with respect to the current modulated by the laser driver (Section 3.1.1) is analyzed in this section, again using the Michelson interferometer setup. The modulating voltage to the laser driver is given by a ramp signal (the value will be divided by 10 by the LabVIEW program (APPENDIX, FIGURE C.1 and FIGURE C.3), goes to the diode driver, where it gets a gain of 2) and the response is observed using the in photodetector when the cube corners are maintained stationary with $x_1 - x_2 = 0.127$ m (flow diagram shown in FIGURE 61). The phase of the signal in the FIGURE 62 is used to calculate the wavelength modulation that occurred. From FIGURE 62, it is clearly seen that the current modulation changes the intensity at the photodetector. The number of fringes observed at the peaks of the ramp is higher than the fringes observed at valleys of the ramp. We had to plot the test from 10 seconds, since the interferometer took that time to stabilize (the fringes were a little distorted by then).

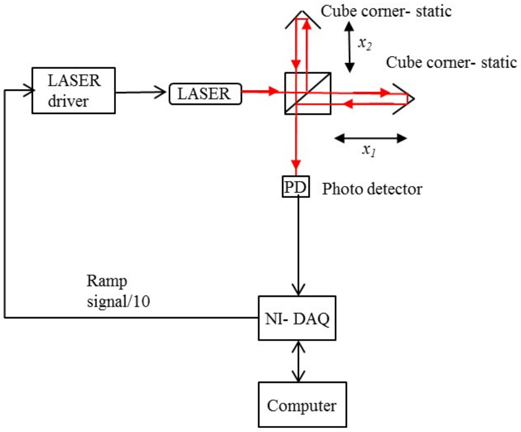

FIGURE 61: Flow diagram- Measurement of wavelength modulation with modulation of current to the laser diode

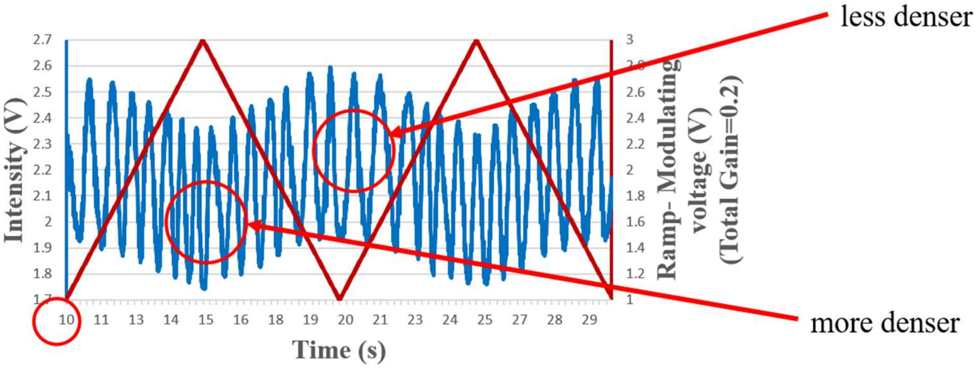

FIGURE 62: Measurement of wavelength modulation with voltage, which is proportional to current through the laser diode

$$\begin{aligned}\phi &= \frac{2\pi\Delta x}{\lambda}\\ &= \frac{2\pi.2(x_1 - x_2)}{\lambda}\\ &= \frac{4\pi(x_1 - x_2)}{\lambda}\end{aligned} \tag{15}$$

Therefore, the change in phase with wavelength is,

$$\frac{d\phi}{d\lambda} = -\frac{4\pi(x_1 - x_2)}{\lambda^2} \tag{16}$$

And also

$$d\phi = m2\pi + \frac{2\pi\left(a + b\right)}{S} \tag{17}$$

Where,

ϕ is the phase of the signal

$x_1 - x_2 = 0.127$ m is half the path length difference

$\lambda = 635$ nm is the central wavelength and

$m = 5$ is the number of complete fringes

$a = 0.3$ is shown in FIGURE 63

b = 0.3 is shown in FIGURE 63

S = 0.6 is shown in FIGURE 63

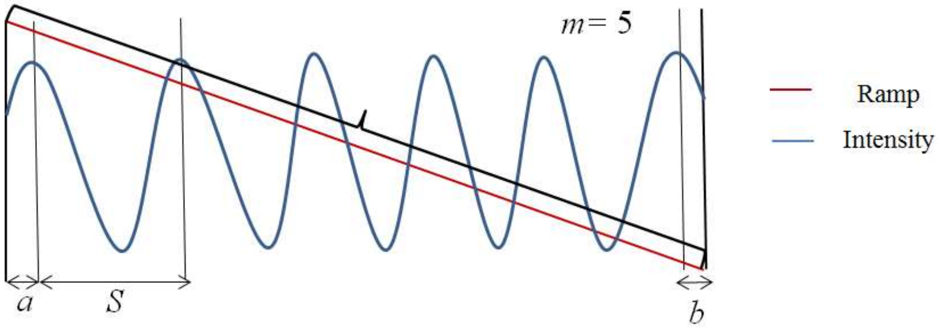

FIGURE 63: Blown-up view- calculation of phase variation

The region marked with curly braces for a descending ramp (FIGURE 63) is used for the varying phase calculation. Equation 17 is used to calculate $d\phi$ (37.7 radians) and equation 16 is used to calculate the modulating wavelength $d\lambda$ as 9.525 pm

As the resistance across the laser diode is 75 Ω and the ramp voltage amplitude which is divided by 10 makes the modulating voltage amplitude 0.2 V after passing the diode driver it becomes 0.4 (gain of 2), the current is calculated as 5.33 mA (0.4 V/ 75 Ω). Thus, the wavelength modulated per ampere is 1.786 nm (9.525 pm/ 5.33 mA). FIGURE 64 shows the drift occurred in the signal observed. In the absence of the drift, we might have observed a sinusoidal wave overlapping on each other (interrogation of this character is a part of the future work). The theory behind the variation of the intensity of light with the phase shift is not included in our model and it will also be a part of the future work.

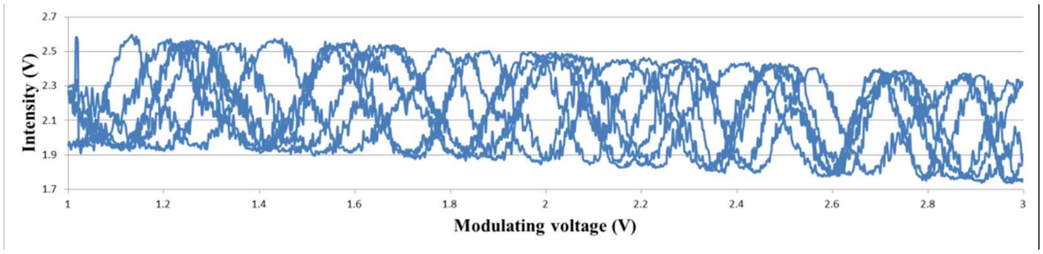

FIGURE 64: Drift in the signal

3.1.3.9 Detection of harmonics

The harmonics of the laser signal are detected (FIGURE 34) using the SR850 DSP lock-in amplifier. As the lock-in amplifier can detect only one harmonic at a time, two lock-in amplifiers are used. The ‘sine out’ source of modulating sine wave to the laser driver from a lock-in amplifier is locked as a reference in the other. The output from the photodetector is connected to the signal inputs of the two amplifiers. The magnitude of the harmonics f , $2f$ and $3f$ are recorded by connecting the phase outputs of the lock-in amplifier to NI-DAQ. The time constant of the lock-in amplifier is 300 ms, their characteristics are observed using the front panel of LabVIEW (FIGURE 35) with different amplitude and frequency of modulating sine wave input to the laser driver.

FIGURE 65 shows that f and $2f$ frequencies are of zero phase difference for the ramp signal to piezo of 1 V, modulating amplitude of 0.566 V (rms value driven from lock-in (V_{rms}) is 0.2, and $V_{peak} = \sqrt{2}\ V_{rms} = 0.283$, and a gain of 2 at the laser driver makes it 0.566), and frequency, f_m = 2 kHz to the laser driver (FIGURE 66). Theoretically, the phase difference should be closer to 90° (interrogation of this behavior is a part of our future work). Although their rotating vector (FIGURE 67) is not a complete circle as the theory in FIGURE 8, the rotating vector of the intensities of f and $2f$ frequencies produce a repeatable trace (FIGURE 68).

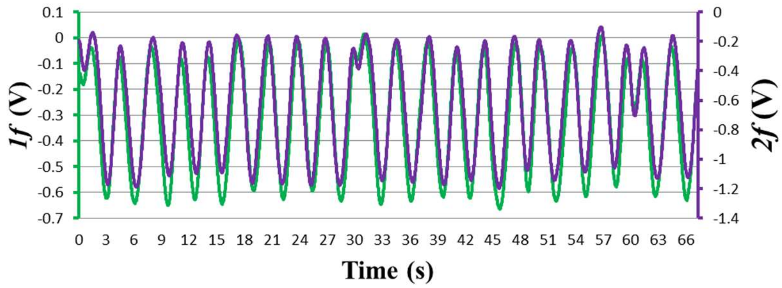

FIGURE 65: f and $2f$ harmonics (δ_m = 0.566 V; f_m = 2 kHz; ramp= 1 V)

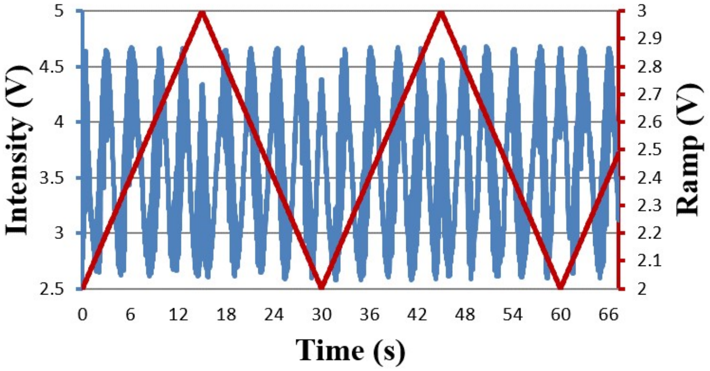

FIGURE 66: Intensity at photodetector (δ_m = 0.566 V; f_m = 2 kHz; ramp = 1 V)

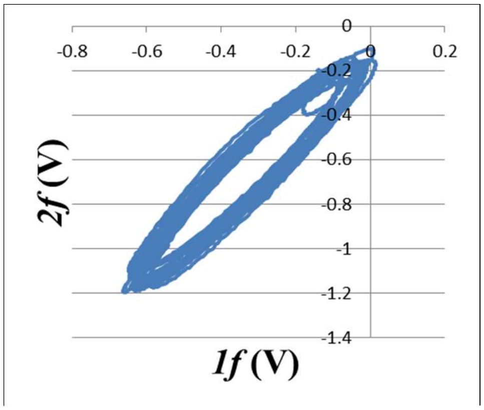

FIGURE 67: Rotating vector (δ_m = 0.566 V; f_m = 2 kHz; ramp = 1 V)

FIGURE 68 shows that the amplitude of f and $2f$ increases with increase in the modulating sine frequency from 2 kHz to 3 kHz but keeping the same modulating amplitude at the laser driver. The f and $2f$ harmonics shows a phase difference of 180° (FIGURE 68) and the rotating vector moved from 4th quadrant to 2nd and the shape shows no improvement (FIGURE 70). We also reduced the ramp amplitude to 0.5 V, to see whether that can make a difference (FIGURE 69).

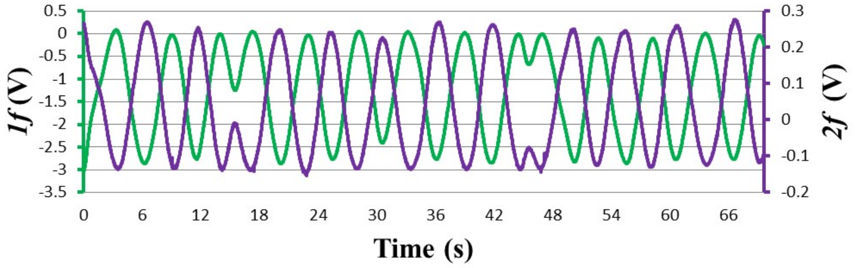

FIGURE 68: f and $2f$ harmonics (δ_m = 0.566 V; f_m = 3 kHz; ramp = 0.5 V)

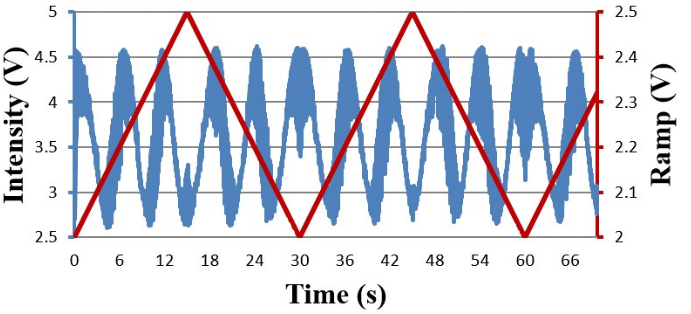

FIGURE 69: Intensity at photodetector (δ_m = 0.566 V; f_m = 3 kHz; ramp = 0.5 V)

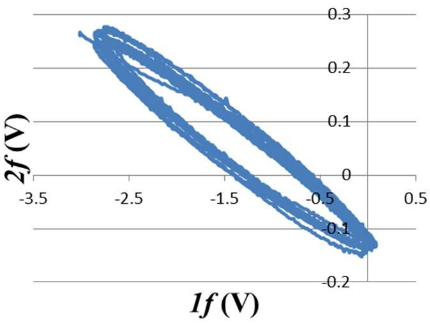

FIGURE 70: Rotating vector (δ_m = 0.566 V; f_m = 3 kHz; ramp = 0.5 V)

FIGURE 71 shows that f and $2f$ frequencies are of 90° phase difference with a decrease in the modulating sine input frequency from 3 kHz to 1 kHz and increasing the modulating amplitude from 0.566 V to 1.414 V (The rms value driven from the lock-in is 0.5 V, current modulation is, 1.414 V/ 75 Ω = 18.85 mA). Although the current modulation ($\pm 18.85\,\mathrm{mA}$) is higher than the upper limit that the laser diode can operate (±15 mA, see Appendix B), the laser worked fine. This may be due to the factor of safety that the manufacturer has employed. The signal gets noisier as the modulating voltage is high (FIGURE 72), which could have affected our results, but the lock-in amplifiers should have got rid of the noises when measuring the f and $2f$ frequencies, thus the shape of the rotating vector got better (FIGURE 72), getting closer to the circle shown in the theory (FIGURE 8).

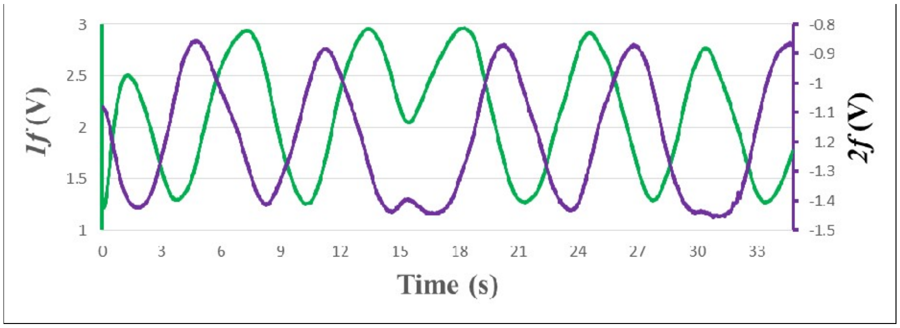

FIGURE 71: f and $2f$ harmonics (δ_m = 1.414 V; f_m = 1 kHz; ramp= 0.5 V)

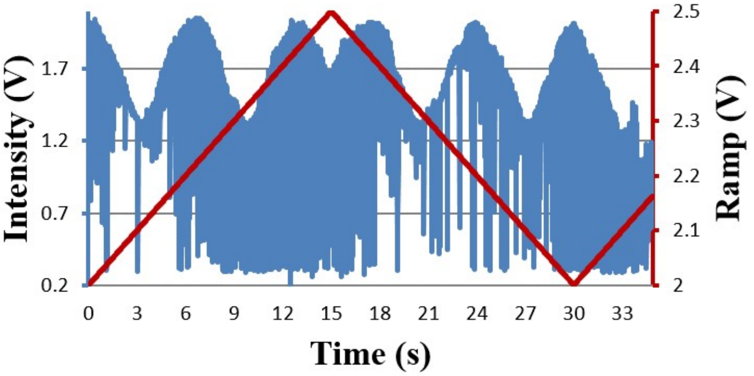

FIGURE 72: Intensity at photodetector (δ_m = 1.414 V; f_m = 1 kHz; ramp= 0.5 V)

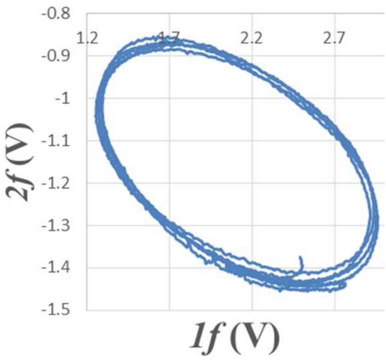

FIGURE 73: Rotating vector (δ_m = 1.414 V; f_m = 1 kHz; ramp= 0.5 V)

We increased the modulating amplitude to 1.697 V (22.62 mA, the laser diode was still able to operate) and observed that the circular shape got smaller (FIGURE 76). f and $2f$ harmonics and the intensity plots are shown in FIGURE 74 and FIGURE 75.

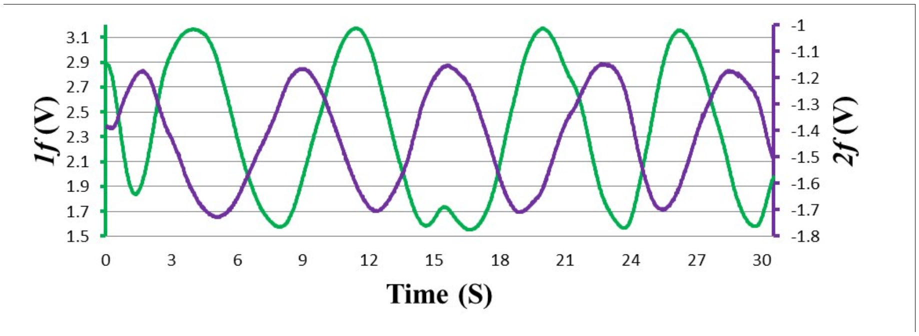

FIGURE 74: f and $2f$ harmonics (δ_m = 1.697 V; f_m = 1 kHz; ramp = 0.5 V)

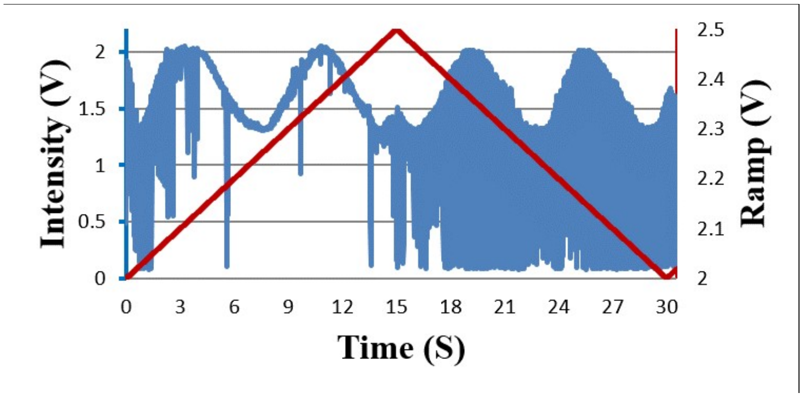

FIGURE 75: Intensity at photodetector (δ_m = 1.697 V; f_m = 1 kHz; ramp = 0.5 V)

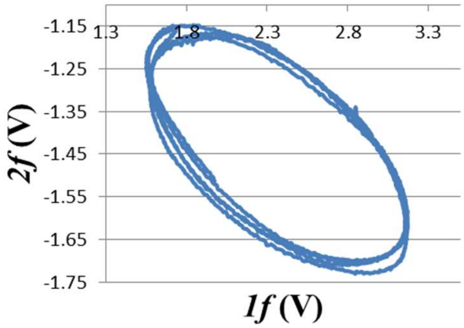

FIGURE 76: Rotating vector (δ_m = 1.697 V; f_m = 1 kHz; ramp = 0.5 V)

We have also observed the behavior of $2f$ and $3f$ harmonics and f and $3f$ harmonics which shows a 90° phase difference (FIGURE 77 and FIGURE 80), though the rotating vectors traces a repeating path, it got much noisier (FIGURE 79 and FIGURE 82).Their intensity responses are shown in FIGURE 78 and FIGURE 81.

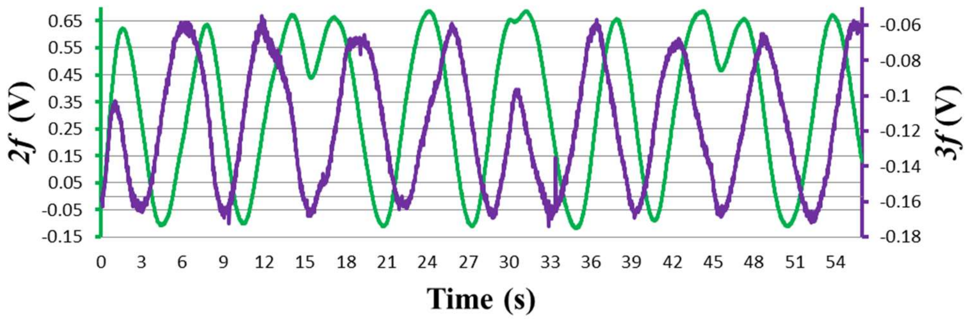

FIGURE 77: $2f$ and $3f$ harmonics (δ_m = 0.566 V; f_m = 3 kHz; ramp = 0.5 V)

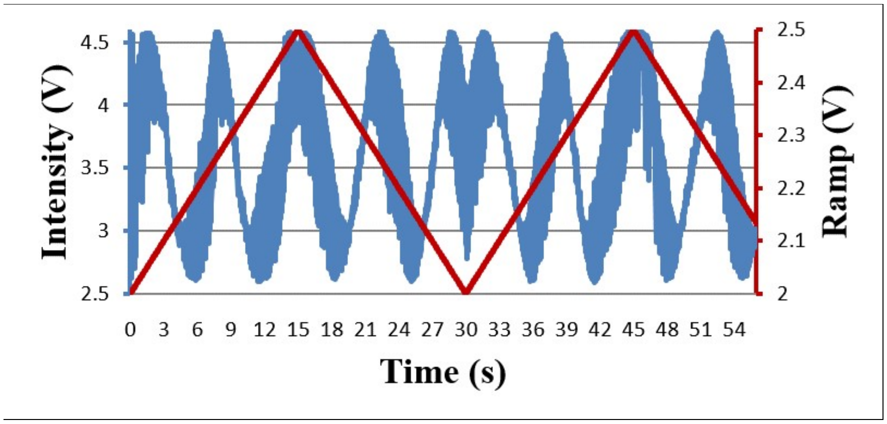

FIGURE 78: Intensity at photodetector (δ_m = 0.566 V; f_m = 3 kHz; ramp = 0.5 V)

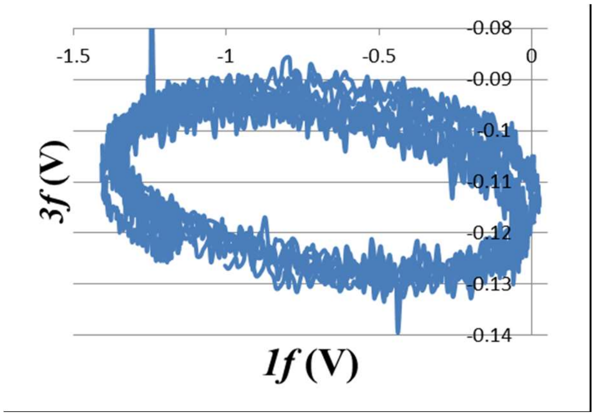

FIGURE 79: Rotating vector (δ_m = 0.566 V; f_m = 3 kHz; ramp = 0.5 V)

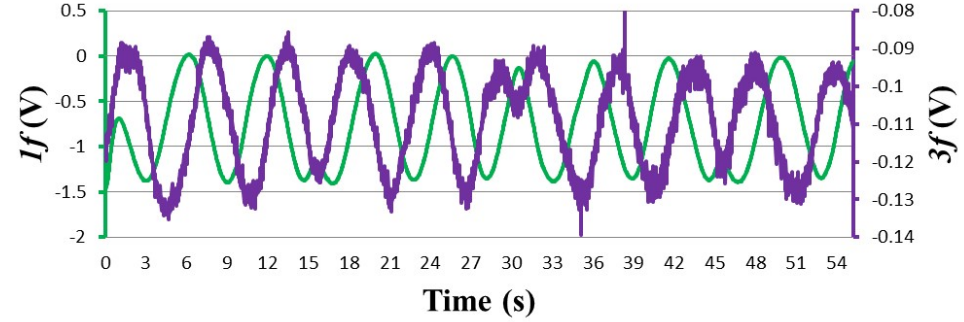

FIGURE 80: f and $3f$ harmonics (δ_m = 0.566 V; f_m = 3 kHz; ramp = 0.5 V)

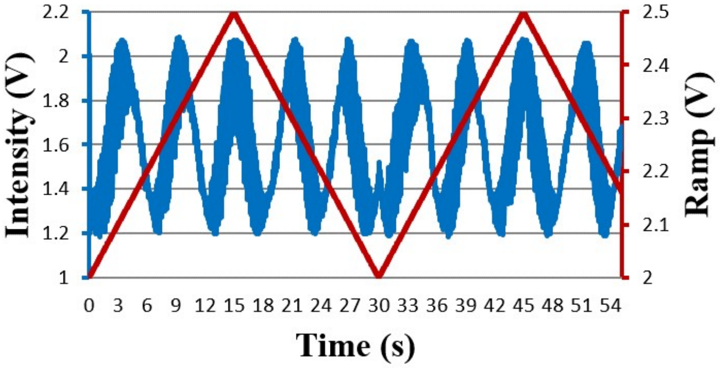

FIGURE 81: Intensity at photodetector (δ_m = 0.566 V; f_m = 3 kHz; ramp = 0.5 V)

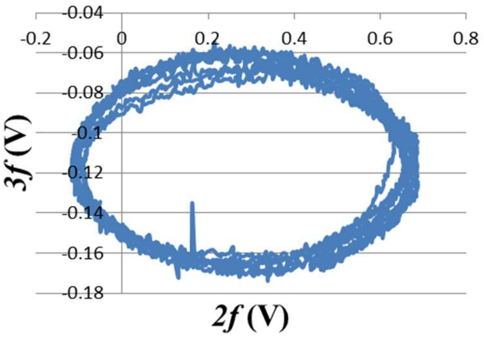

FIGURE 82: Rotating vector, (δ_m = 0.566 V; f_m = 3 kHz; ramp = 0.5 V)

3.1.3.10 Modulation depth- Bessel function

Bessel function, $J_n(\delta)=\sum_{k=0}^{\infty}\frac{(-1)^k(\delta/2)^{2k+n}}{k!(k+n)!}$ represents the harmonics of a signal with modulation amplitude (δ). FIGURE 83 shows the Bessel function plot of the fundamental and the first three harmonics. The modulation depth (δ) value corresponds to the ratio of the harmonics observed (from FIGURE 68, FIGURE 71, FIGURE 74, FIGURE 77 and FIGURE 80) is 1.28. FIGURE 84 shows a clear representation of the ratio of the harmonic amplitudes of f , $2f$ and $3f$.

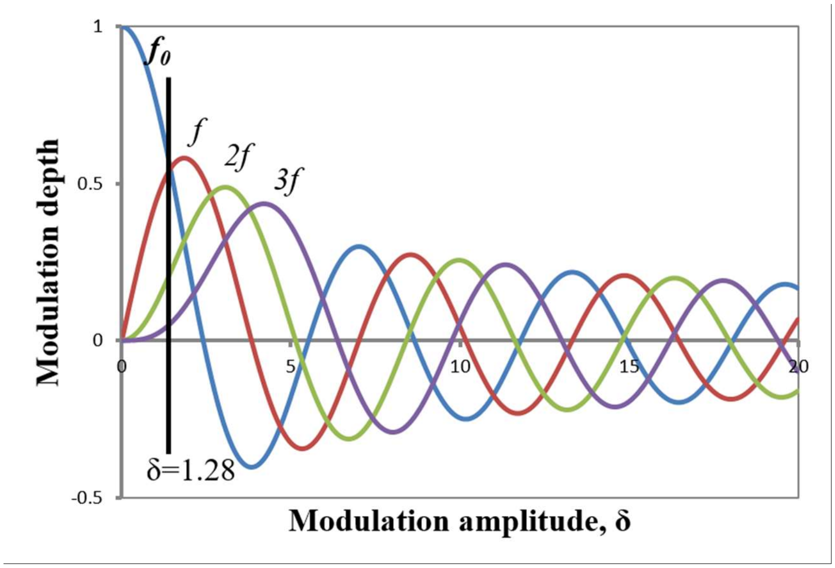

FIGURE 83: Bessel function

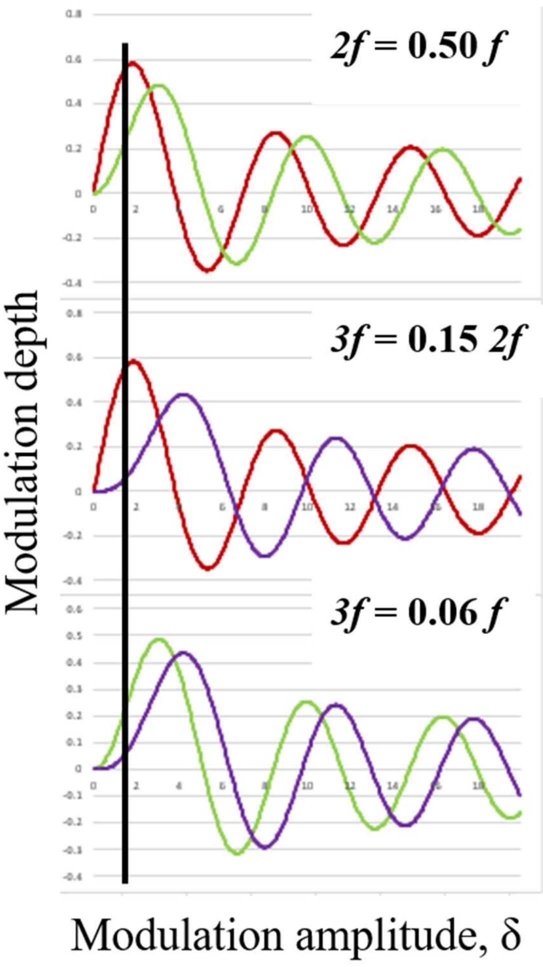

FIGURE 84: Ratios of harmonics

CHAPTER 4: CONCLUSIONS AND FURTHER WORK

4.1. Conclusion

From this work we have investigated the mathematical model developed by Wilkinson and Pratt [1] by using a Michelson interferometer. Rotating vector representation of the first and second harmonics of the intensity is achieved using Jacobi-Anger transform and Fourier coefficients. A real time DAQ system is used in initiating and measuring the displacement of the cube corner in combination with a photodetector detecting the varying intensity. Experimental setup built is calibrated using a capacitance displacement sensor. The Resolution of the setup is established by using the rotating vector shown in FIGURE 50. The wavelength modulation of the laser diode (nominal wavelength, 635 nm) is achieved by modulating the current through the laser diode using a laser driver (FIGURE 62). Coherence length of the laser is found by varying the path length difference and observing the changes in fringe visibility. The rotating vector representation of the modulation harmonics f , $2f$ and $3f$ in the signal are evaluated with different modulating amplitudes and frequencies using DAQ. The phase shift of the harmonics is different from what the theory suggested (theory says, 90°). Since the optical system used for the simple Michelson interferometer did not have an optical isolator, the beam returning back to the laser diode might have caused the instability in signal. Exploring the reason for varying phase difference and noise in the system, drift in the signal, improving the amplitude of the wavelength modulation achieved, intensity variation with phase shift and building a Fabry-Perot interferometer and comparing its experimental results with the theoretical results will be our future work.

4.2. Further Work

As the wavelength modulated per ampere achieved is low (3.65 nm/A), we built a flexure assembly to modulate the wavelength by inducing stress on the laser crystal. We have also manufactured a cylinder housing a focusing lens, which will be a part of the optical arrangement for the Fabry-Perot interferometer.

4.2.1. Frequency Modulation by Induction of Stress on Laser Crystal

Applying stress over the area of laser crystal will modulate the wavelength of the light from the laser diode. A flexure mechanism, FIGURE 86, is modeled and manufactured to apply the stress over the crystal with the needle. The disadvantages involved are that the surface area of crystal is too small to access (0.05 mm^2 shown in FIGURE 85 measured using the microscope with Infinity 2 camera) and it is covered with gold coating. The needle might also interrupt the wires emanating from the crystal resulting in short circuit. The future plan is to build a laser crystal of larger surface area.

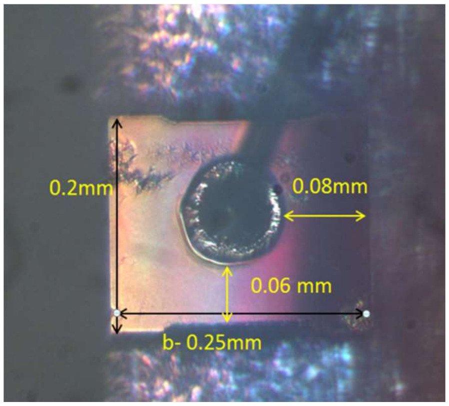

FIGURE 85: Laser crystal

4.2.2. Flexure Assembly

The modeled flexure shown in FIGURE 86 has 4 leaf flexures actuated by Piezo electric crystal displacing it in z axis. This motion will get the laser diode crystal poked by the needle. The stage carrying the diode displaces in *x* direction by sliding and in the *y* direction using bolts, and the needle is set in place using set screw

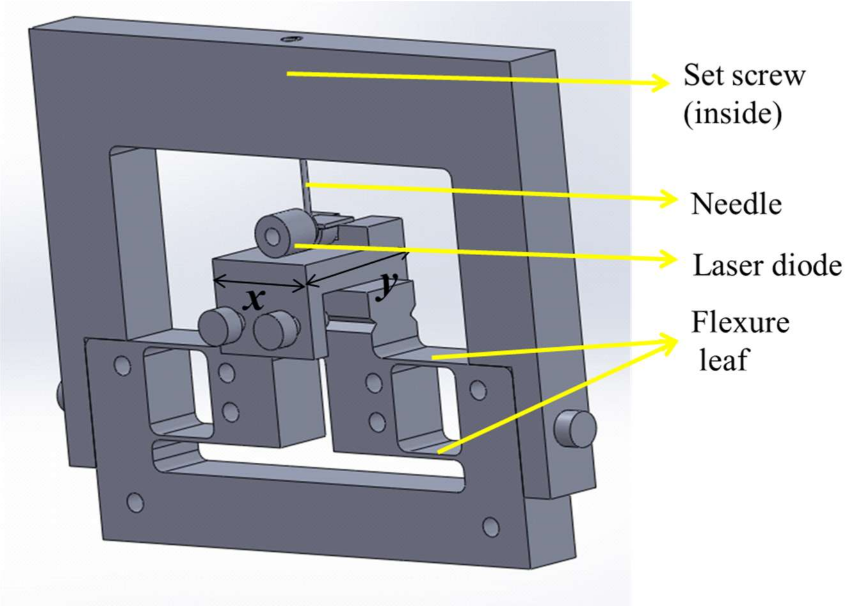

FIGURE 86: Flexure assembly

Strain,

$$\varepsilon = \left(\frac{\sigma}{E}\right)\nu = \left(\frac{F/A}{E}\right)\nu \tag{18}$$

Therefore, Force to be applied on the crystal,

$$F = \left(\frac{E\varepsilon A}{\nu}\right) = 21 \text{ N}$$

Where,

ε = 10^{-3} Pa is the strain (say)

ν is the Poisson's ratio= 1/3 (say)

E is the Young's modulus= 140 GPa (for Silicon)

A is the area of the crystal= 0.050 mm^2

4.2.3. The Design of Leaf Spring Flexure

Thickness,

$$t = \left(\frac{Fl^3}{Ebx} \right)^{1/3} = 0.88 \text{ mm}$$

Where,

Width, b= 8 mm (say)

Length, l= 12 mm (say)

Young's modulus, E= 120 GPa (for Aluminum)

Total deflection, x = 60 µm (50 µm for preload and 10 µm for additional deflection)

Yield stress, $\sigma_y = \frac{6Ex}{l^2}$ = 18 MPa <<100 MPa

The flexure assembly manufactured using Bridgeport and Smithy machines is shown in FIGURE 87.

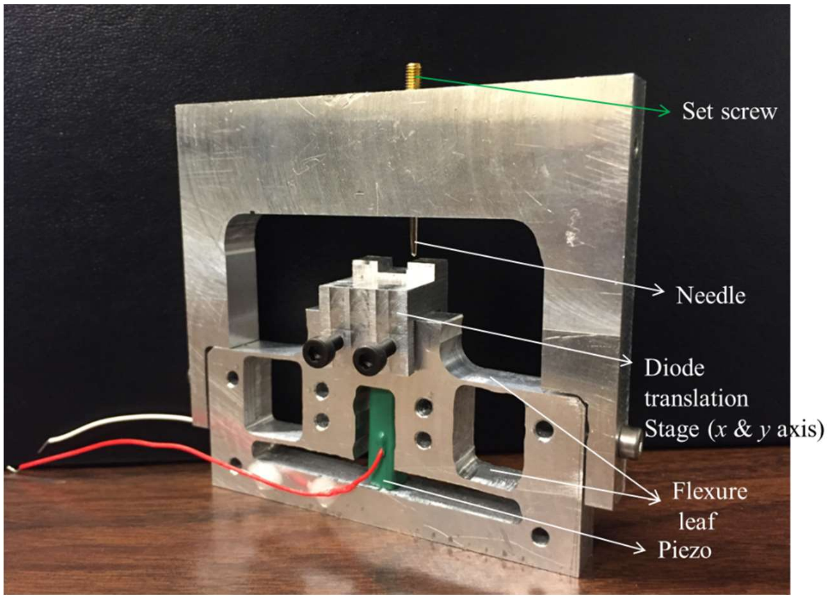

FIGURE 87: Manufactured flexure assembly

4.2.4. Optical System for Fabry- Perot Interferometer

The optical system (FIGURE 88) for the Fabry- Perot interferometer setup consists of a current modulated laser diode with its beam coupled in to the fiber through a convex lens (Planovex plastic lens Comar 33PP09, 32.7 mm focal length and 9 mm diameter) and an optical isolator. The optical isolator will avoid the light travelling back to the laser diode, thus stabilizing the signal. The laser diode is mounted at the open end of the cylinder shown in FIGURE 89 with the lens glued to its other side.

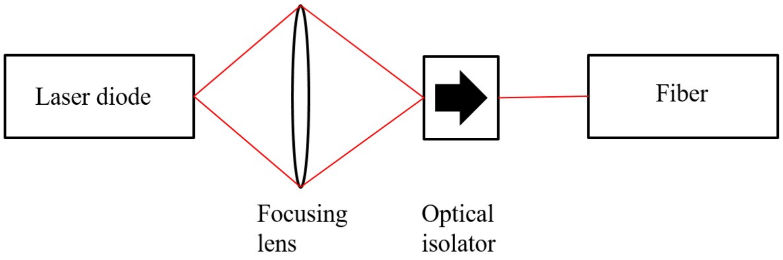

FIGURE 88: Optical system for Fabry- Perot interferometer

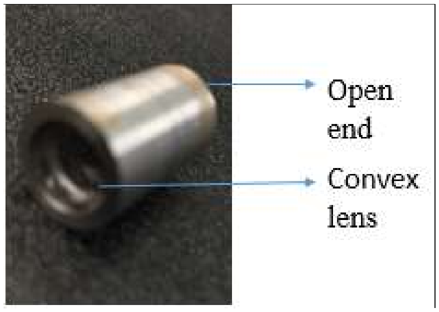

FIGURE 89: Laser mounting cylinder with lens

The ends of the fiber in the coupler are cleaved to increase the intensity of the beam to be sensed by the photodetector. The beam will be sent through the first end of the fiber coupler (FIGURE 90). The outputs from ends 2 and 3 will get reflected from the target and sensed by photodetector respectively as illustrated in FIGURE 3.

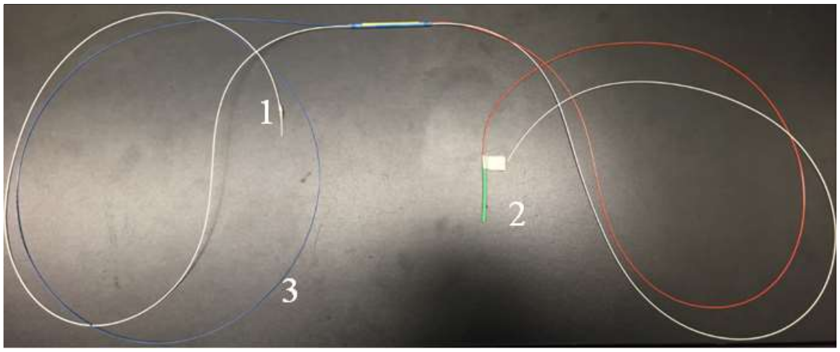

FIGURE 90: Fiber coupler

REFERENCES

[1] Paul R. Wilkinson and Jon R. Pratt, “Analytical model for low- finesse, external cavity, fiber Fabry- Perot interferometers including multiple reflections and angular misalignment” 10 August 2011/ Vol. 50, No. 23/ Applied Optics.

[2] Bartosz K. Nowaskowski, Douglas T. Smith and Stuart T. Smith, “Development of a miniature, multichannel, extended, range Fabry- Perot Fiber- Optic Laser Interferometer system for low frequency Si-traceable displacement measurement” Downloaded on 11 June 2015.

[3] Eric D. Black, “An introduction to Pound- Drever- Hall laser frequency stabilization”, Am. J. Phys., Vol. 69, No. 1, January 2001.

[4] Klaus Thurner, Pierre- Francois Braun and Khaled Karrai, “Absolute distance sensing by two laser optical interferometry”, Review Of Scientific Instruments 84, 115002 (2013).

[5] Siming Feng and Herbert G. Winful, “Physical origin of the Gouy phase shift”, April 15, 2001/ Vol. 26, No. 8/ Optics Letters.

[6] Haider I. Rasool, Paul R. Wilkinson, Adam Z. Stieg and James K. Gimzewski, “A low noise all- fiber interferometer for high resolution frequency modulated atomic force microscopy imaging in liquids”, Review Of Scientific Instruments 81, 023703 (2010).

[7] D Hunger, T. Steinmetz, Y Colombe, C Deutsch, T W Hansch and J Reichel, “A fiber Fabry- Perot cavity with high finesse”, New Journal of Physics 12, (2010) 065038.

[8] S. Nemoto and T. Makimoto Analysis of splice loss in single- mode fibres using a Gaussian field approximation, Optical and Quantum Electronics 11 (1979) 447-457.

[9] G.N. Watson, A treatise on the theory of Bessel functions

[10] Francis B. Hildebrand, Advanced calculus for applications

APPENDIX A: MATLAB Code

A.1. Main function: ReflFourierCoeffvaryingLambda.m

```
clc
clear all

%####### Set up parameters for array calculation  #########
rm=0.2; % Mirror reflectance
Theta=0.0001; % misalignemnt of cavity mirror
N=5; % number of terms in the series (reflections)
lambdacarrier=1550e-9; % Wavelength of source (carrier)
zstart=150e-6; % start of x axis (separation)
zstop=155e-6; % End of x axis (separation)% enter 1550 nm
moddepth=0.05E-9; %depth of modulation % enter 0.05 nm
zdatapoints=5000; % Number of datapoints in the plots
zinc=(zstop-zstart)/(zdatapoints-1); % z separation between data points
fm=1200;%frequency of modulation in Hz
omegam=2*pi*fm;%frequency of modulation in rad per sec
tdatapoints=50;
tstart=0;
tstop=1/fm;
tinc=(tstop-tstart)/(tdatapoints-1); %time increment


for ii=1:zdatapoints
    a1temp=0;
    b1temp=0;
    delz=(ii-1)*zinc;
    z(ii)=zstart+delz;

    for iii=1:tdatapoints
    t(iii)=tstart+(iii-1)*tinc;
    dellambda=moddepth*sin(omegam*t(iii)); %modulation of wavelength
    lambda(iii)=lambdacarrier+dellambda;
    [R(ii)]=Rarraycreator(z(ii),Theta, N, rm, lambda(iii)); %R is the
intensity

%######To find Fourier coefficients#########
    a1(ii)=R(ii)*cos(2*pi*iii/(tdatapoints-1));
    b1(ii)=R(ii)*sin(2*pi*iii/(tdatapoints-1));

    a1(ii)=a1temp+a1(ii);
    b1(ii)=b1temp+b1(ii);

    a1temp=a1(ii);
    b1temp=b1(ii);

    end

end
a1=a1/(tdatapoints-1);
b1=b1/(tdatapoints-1);
```

```
figure(1)
plot(z*1000000,R)
title('Intensity as a function of mirror separation','FontName','Times
New Roman','FontSize',15,'Color','k')
xlabel('Separation (\mum)','FontName','Times New
Roman','FontSize',15,'FontWeight','bold','Color','k')
ylabel('Intensity (arb.)','FontName','Times New
Roman','FontSize',15,'FontWeight','bold','Color','k')

figure(2)
plot(z*1000000,a1)
hold on
plot(z*1000000,b1,'k')
title('Intensity of Fourier coefficients as a function of
separation','FontName','Times New Roman','FontSize',15,'Color','k')
xlabel('Separation (\mum)','FontName','Times New
Roman','FontSize',15,'FontWeight','bold','Color','k')
ylabel('Intensity* Fourier coefficients (arb.)','FontName','Times New
Roman','FontSize',15,'FontWeight','bold','Color','k')
legend('a1','b1')

figure(3)
title('Rotating vector representation','FontName','Times New
Roman','FontSize',15,'Color','k')
plot(a1,b1)
xlabel('I_f','FontName','Times New
Roman','FontSize',15,'Fontangle','italic','Color','k')
ylabel('I_2_f','FontName','Times New
Roman','FontSize',15,'Fontangle','italic','Color','k')

figure(4)
title('Rotating vector representation 3D','FontName','Times New
Roman','FontSize',15,'Color','k')
plot3(a1,b1,z)
xlabel('I_f','FontName','Times New
Roman','FontSize',15,'Fontangle','italic','Color','k')
ylabel('I_2_f','FontName','Times New
Roman','FontSize',15,'Fontangle','italic','Color','k')
zlabel('Separation (\mum)','FontName','Times New
Roman','FontSize',15,'FontWeight','bold','Color','k')

figure(5)
title('Wavelength modulation','FontName','Times New
Roman','FontSize',15,'Color','k')
plot(t,lambda)
axis([0 1/fm 1549.95e-9,1550.05e-9 ])
xlabel('Time','FontSize',15,'FontName','Times New
Roman','FontSize',15,'Color','k')
ylabel('Modulated wavelength ( \lambda)','FontName','Times New
Roman','FontSize',15,'Color','k')
```

A.2. Function Rarraycreator.m

```
function[R] =Rarraycreator(z,Theta, N, rm, lambda)

 % This function computes the array of theoretical reflectivity over
the z range of wavelength values
lambdadatapoints=length(lambda);

for ii=1:lambdadatapoints
  [R(ii)]=FPfiberfuncRmvaryinglambdaKA(z(ii),Theta,N, rm, lambda(ii));
end
end
```

A.3. Function FPfiberfuncRmvaryinglambdaKA.m

```
function [R15] =FPfiberfuncRmvaryinglambdaKA(z,Thetam,N, rm, lambda)

i=sqrt(-1); % obvious
nc=1; % Refractive index of the medium between fibers (nc=1 for air)
s=3.7e-6; % Spot radius

%######### Major parameter for mirror alignment #########
Co=1; % being equivalent ot a perfect cleave.

ThetaCritical=0.2; %Critical angle for total internal reflect
                   %(in this case a lower value is chosen assumimg that
                   %intensities are 'walking' out of the gap fairly
fast.
                   %Not used in this program

%############ Number of reflections
#####################################
k=2*pi*nc/lambda; % Wavevector
zR=1.414*k*s*s; %Rayleigh length 1.414 factor comes from prior analysis
ro=0.2; % Field reflectivity from inside the fiber if nuo=1.5 nu=1
ro=((nuo-nu)/(nuo+nu))=0.2
to=sqrt(1-ro^2); % Transmision from inside the fiber
rodash=0.2; % Field reflectivity from the fiber from light impinging
from the medium (air).
todash=sqrt(1-rodash^2); % Transmission of light into the fiber from
the medium (air).
zm=z/zR;

%############# Determining the terms in equation (15)
###################
% This loop nest is for computing the third term in equation (15)
   innertemp2=0;
for ll=1:N
    innertemp3=0;
    [yy,xx,ww]=Ccoeffsm(k,zR,ll,Thetam,zm);
        delta(ll)=yy;
        betan(ll)=xx;
        THETA(ll)=ww;
   for nn=ll+1:N
```

```
        [yy,xx,ww]=Ccoeffsm(k,zR,nn,Thetam,zm);
        delta(nn)=yy;
        betan(nn)=xx;
        THETA(nn)=ww;
        Cn(nn)=delta(nn)*exp(-i*betan(nn))*exp(-i*THETA(nn));

Thirdterm=(2*(to^4)/(ro^2))*((rm*ro)^(nn+ll))*delta(nn)*delta(ll)*cos(b
etan(nn)-betan(ll)+THETA(nn)-THETA(ll))+innertemp3;
    innertemp3=Thirdterm;
   end
   innertemp2=innertemp3+innertemp2;
end
sumthirdterm=innertemp2;

% this loop computes the first and second terms in equation (15)
    sumfirst=0;
    innertemp=0;
    for nn=1:N
     [yy,xx,ww]=Ccoeffsm(k,zR,nn,Thetam,zm);
        delta=yy;
        betan=xx;
        THETA=ww;

sumsecond=(2*to*to)*((rm*ro)^nn)*delta*cos(betan+THETA+pi)+innertemp;
        innertemp=sumsecond;
        sumfirst=((to^4)/(ro^2))*((rm*ro)^(2*nn))*delta^2+sumfirst;
    end
R15=ro*ro+sumfirst+sumsecond+sumthirdterm; % intensity
end
```

A.4. Function Ccoeffsm.m

```
function [ delta, betan, THETAm ] = Ccoeffsm( k,zr,n,thetam,zmbar )
%These are the oceefficients computed from equation 12 in Pauls paper
%   Very simple
betan=2*n*k*zmbar*zr;
THETAm=-atan(n*zmbar)+(n*n*thetam*thetam*k*zr*(3*n*zmbar-
(n*zmbar)^3)/(1+n*n*zmbar*zmbar));
delta=(1/sqrt(1+n*n*zmbar*zmbar))*exp(-
k*zr*n*n*thetam*thetam*(1+5*(n*zmbar)^2)/(1+(n*zmbar)^2));
end
```

APPENDIX B: Datasheet- Laser Diode

MODEL TYPE

VLM-635-03 LPA / VLM-650-03 LPA

OUTLINE DIMENSIONS (UNITS: mm)

Outline

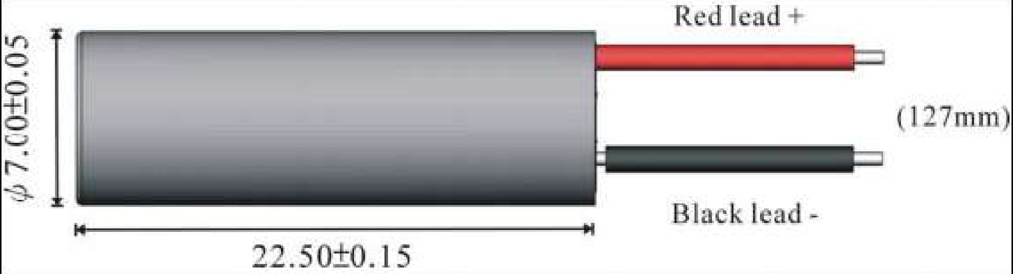

Cross-section profile

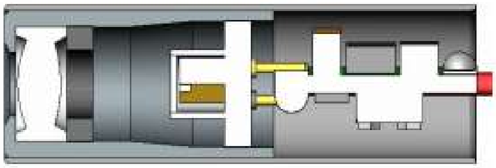

1. For general laser sighting application.
2. This model integrated optic, laser diode, and the APC driver circuit .
3. Options: Connection type: Spring / Lead wire (Spring type: by order).
   Output power: Class II-less than 1mW / Class IIIa – less than 5mW.
4. E.S.D. protection 15KV.

SPECIFICATIONS	635-03	650-03
Operating voltage (Vop)	3~5V	
Operating current (Iop)	40±15mA	
Cw output power (Po)	≦2.5mW	
Wavelength at peak emission (λ p)	630~645nm	645~665nm
Collimating lens	Aspherical plastic (φ 5)	
Housing	Zinc alloy	
Spot size at 5M	6±2mm	
Divergence	2mrad	
Mean time to failure (MTTF) 2.5mW 25℃	5000hrs	10000hrs
Operating temp. range	+10℃~+30℃	
Storage temp. range	-20℃~+65℃	

APPENDIX C: LabVIEW Block Diagrams

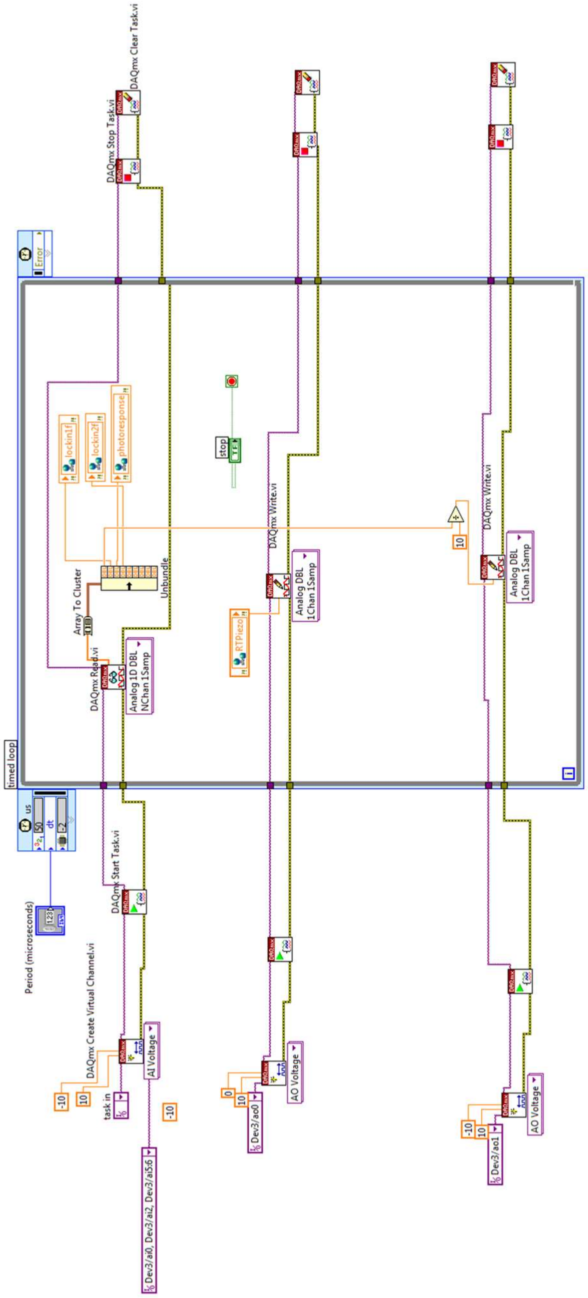

FIGURE C.1: Real time LabVIEW program

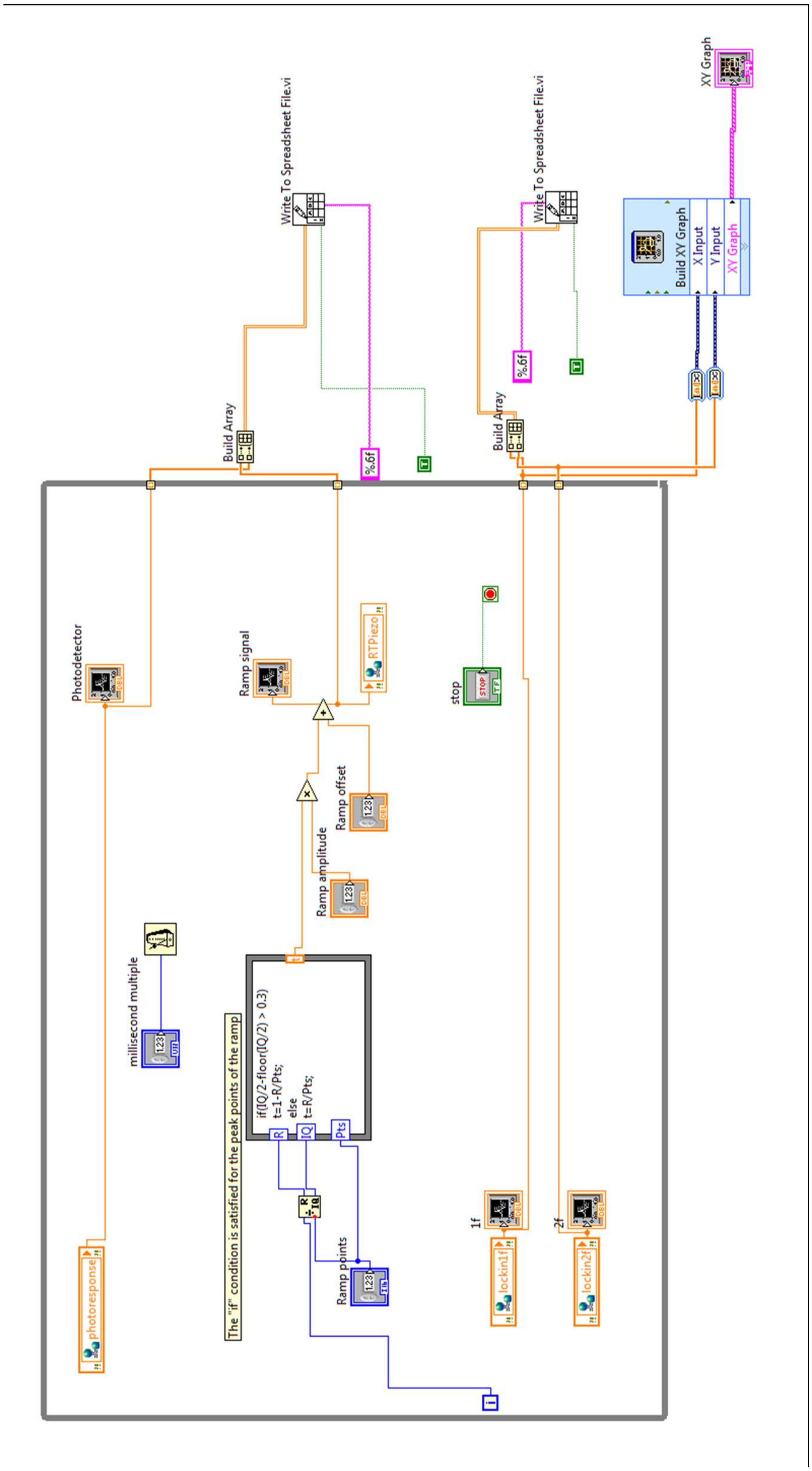

```
if(IQ/2-floor(IQ/2) > 0.3)
t=1-R/Pts;
else
t=R/Pts;
```

FIGURE C.2: Detection of the harmonics of signal

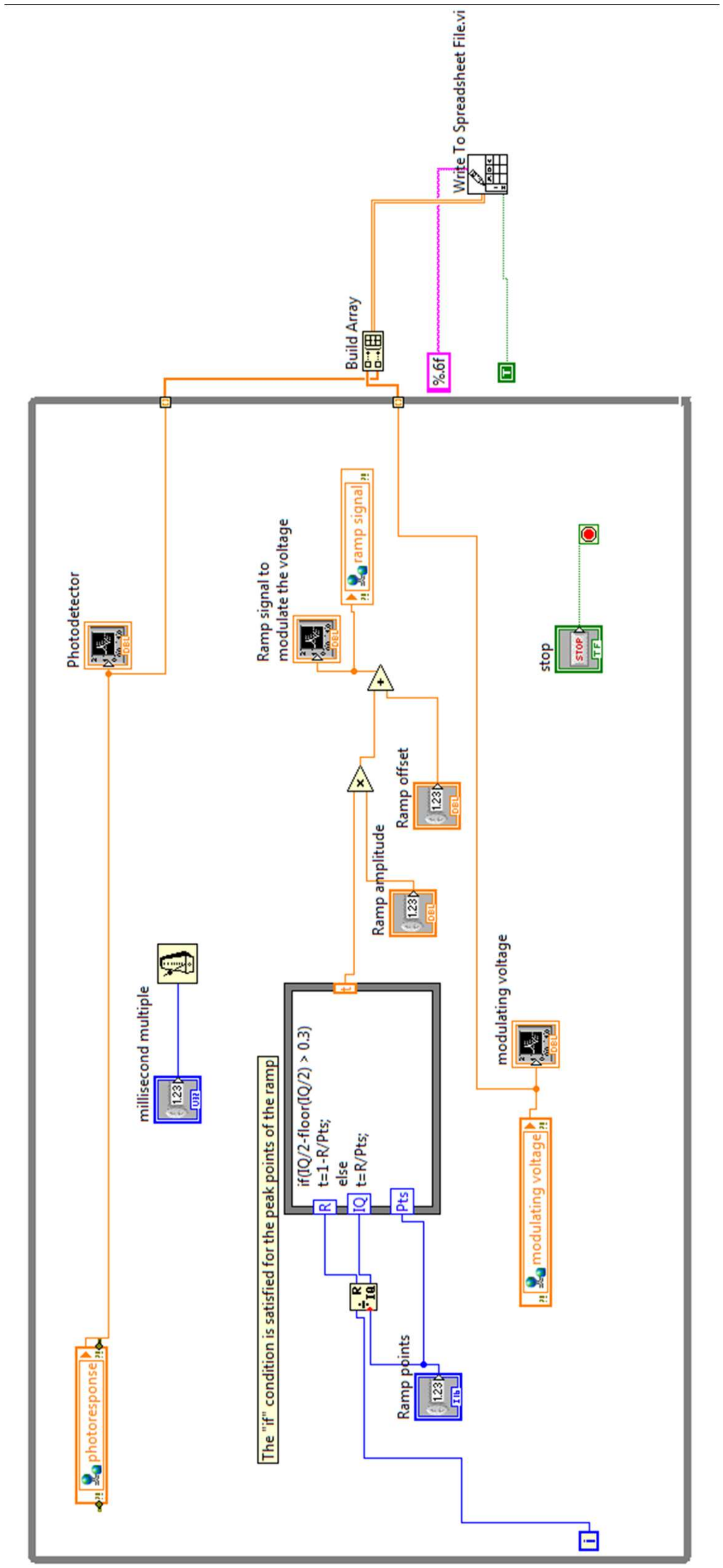

```
if(IQ/2-floor(IQ/2) > 0.3)
   t=1-R/Pts;
   else
   t=R/Pts;
```

FIGURE C.3: Wavelength modulation analysis